iScience

Article

# Female mice lacking GluA3 show early onset of hearing loss, cochlear synaptopathy, and afferent terminal swellings in ambient sound levels

## Graphical abstract

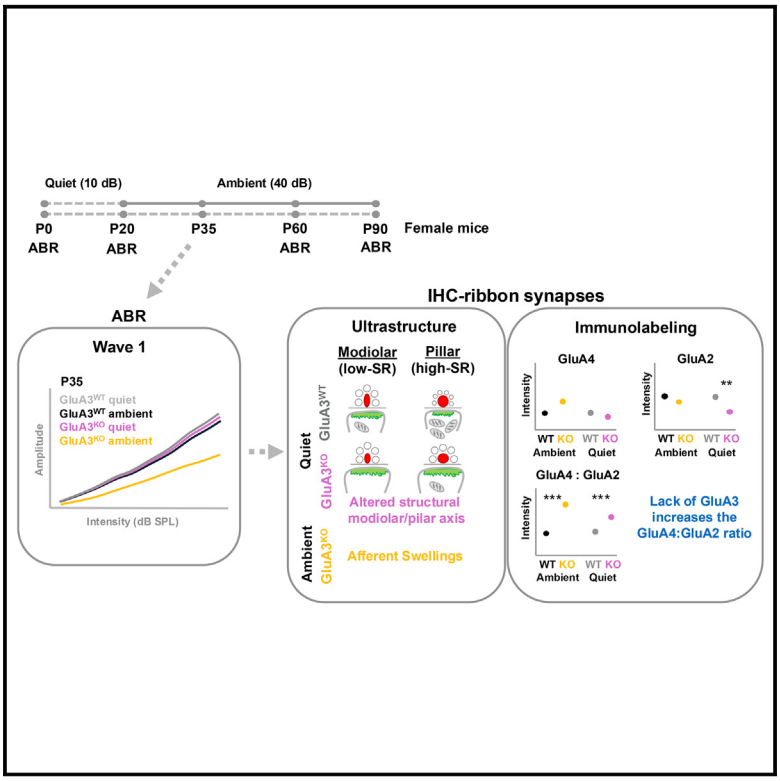


## Highlights

- Cochlear synaptopathy is augmented by ambient sound levels in female GluA3$^{KO}$
- Cochlear dysfunction in ambient sound is prevented by rearing in quiet
- Lack of GluA3 increases the GluA4:GluA2 expression ratio at IHC ribbon synapses
- GluA3 is essential in pre- and post-synaptic development and structural maturation

## Authors

Indra Pal, Atri Bhattacharyya, Babak V-Ghaffari, Essence Devine Williams, Maolei Xiao, Mark Allen Rutherford, María Eulalia Rubio

## Correspondence

mer@pitt.edu

## In brief

Neuroscience; Cellular neuroscience; Sensory neuroscience

Pal et al., 2025, iScience *28*, 111799
February 21, 2025 
https://doi.org/10.1016/j.isci.2025.111799

CellPress

iScience

CellPress
OPEN ACCESS

Article

# Female mice lacking GluA3 show early onset of hearing loss, cochlear synaptopathy, and afferent terminal swellings in ambient sound levels

Indra Pal,[1] Atri Bhattacharyya,[2] Babak V-Ghaffari,[2] Essence Devine Williams,[1] Maolei Xiao,[2] Mark Allen Rutherford,[2] and María Eulalia Rubio[1,3,4,*]

[1]Department of Neurobiology, University of Pittsburgh School of Medicine, Pittsburgh, PA 15261, USA
[2]Department of Otolaryngology, Washington University School of Medicine, St. Louis, MO 63110, USA
[3]Department of Otolaryngology, University of Pittsburgh School of Medicine, Pittsburgh, PA 15261, USA
[4]Lead contact
*Correspondence: mer@pitt.edu
https://doi.org/10.1016/j.isci.2025.111799

## SUMMARY

AMPA-type glutamate receptors (AMPARs) mediate excitatory cochlear transmission. However, unique roles of AMPAR subunits are unresolved. Lack of subunit GluA3 (*Gria3*$^{KO}$) in male mice reduced cochlear output by 8 postnatal weeks. Here, we studied the role of X-linked *Gria3* in cochlear function and synapse anatomy in females. Auditory brainstem responses (ABRs) were similar in 3-week-old female *Gria3*$^{WT}$ and *Gria3*$^{KO}$ mice raised in quiet. However, after switching to ambient sound, ABR thresholds were elevated and wave-1 amplitudes were diminished at 5-week and older in *Gria3*$^{KO}$. A quiet vivarium precluded this effect. Paired synapses were similar in number, but lone ribbons and ribbonless synapses were more frequent, and swollen afferent terminals were observed only in female *Gria3*$^{KO}$ mice in ambient sound. Synaptic GluA4:GluA2 ratios increased relative to *Gria3*$^{WT}$, particularly in ambient sound, suggesting an activity-dependent increase in calcium-permeable AMPARs in *Gria3*$^{KO}$. We propose that lack of GluA3 induces a sex-dependent vulnerability to AMPAR-mediated excitotoxicity.

## INTRODUCTION

The α-amino-3-hydroxy-5-methyl-4-isoxazolepropionic acid receptors (AMPARs) are tetrameric glutamate-gated ion channels with pore-forming subunits GluA1-4 encoded by a family of genes, *Gria1-4*. Each subunit contributes to ionic permeability, pharmacological sensitivity, intracellular trafficking, synapse development, and activity-dependent plasticity of the channel. GluA1 and GluA2 are the most abundant subunits, relatively ubiquitous in the central nervous system, and prominently determine AMPAR plasticity and function, respectively.[1–3] In particular, the absence of GluA2 from the AMPAR tetramer increases the unitary current and makes it permeable to $Ca^{2+}$ in addition to $Na^{+}$ ions. In the adult hippocampus and cortex, the canonical $Ca^{2+}$-permeable AMPAR (CP-AMPAR) involved in synaptic plasticity is the GluA1 homomeric channel. GluA3 and GluA4 have more unique expression patterns, tending to be found at synapses with relatively fast kinetics, such as those in the cochlea and auditory brainstem.[4–6] Interestingly, the mature cochlea and auditory brainstem do not express GluA1, but they do express CP-AMPARs composed of GluA3 and GluA4 subunits.

In male mice, the pore-forming subunit GluA3 of the AMPAR is essential for the development and maintenance of the cochlear afferent "ribbon" synapses that underlie hearing function. Wild-type and GluA3$^{KO}$ mice raised in ambient sound levels had similar hearing sensitivities at one month of age, although ribbon synapses already exhibited ultrastructural and molecular alterations. These alterations include defective position-dependent maturation of pre- and post-synaptic specializations along the inner hair cell modiolar-side to pillar-side morphological axis of structural and functional differentiation, as well as an imbalance of post-synaptic GluA subunit expression—an increase in GluA4 and decrease in GluA2—suggesting a shift toward larger unitary current and greater permeability to $Ca^{2+}$.[6] At 2 months, the cochleae of male GluA3$^{KO}$ mice were less sensitive to suprathreshold sounds (lower wave-1 amplitude of the auditory brainstem response [ABR]), and by 3 months of age, they were less excitable by low-level sounds[7] (elevated ABR threshold). These results showed that synaptic anatomical defects preceded synapse dysfunction leading to hearing loss in male mice lacking GluA3, suggesting a synaptic vulnerability associated with AMPA receptor subunit imbalance in postnatal development that resulted in functional impairment of the mature cochlea.

A non-invasive functional assay of cochlear afferent transmission is wave-1 of the ABR, reflecting synchronous action potential generation in the auditory nerve at the onset of sound. With louder sounds, ABR wave-1 becomes larger. As synapses are lost or the spikes they evoke become less synchronous, ABR wave-1 becomes smaller. In adult mice, females have larger wave-1 amplitudes than males.[8–10] Also, female synapses

appear to be more resistant to noise trauma, and their wave-1 amplitudes are more resistant to reduction in size following noise trauma[9,11]; these sex differences seem related to estradiol. However, the effector molecules mediating these differences have yet to be discovered. Analysis of sex-dependent mRNA expression in the mouse cochlea suggests that *Gria2–4* levels were similar overall but that females had more neurons with higher *Gria3* mRNA relative to *Gria2* and a greater abundance of fast-gating *flop* isoforms.[8] Interestingly, in humans and rodents, *Gria3* is located on the X chromosome,[8,12] where, at least in fibroblasts, the gene is subject to X-inactivation. Here, we studied adolescent and mature female GluA3$^{KO}$ mice raised in an ambient or low-level sound vivarium. We find that female mice are more sensitive to the absence of GluA3 than male mice. Indeed, raising female mice in a vivarium with normal ambient levels of sound resulted in early cochlear synaptopathy and hearing loss, whereas this effect was prevented by rearing in a low-level sound vivarium. In ambient sound, like males, cochlear synapses in female *Gria3$^{KO}$* mice had less GluA2 and more GluA4 relative to *Gria3$^{WT}$*. Thus, cochlear synapses rely on GluA3 subunits for proper structure and function, and we conclude that females depend on GluA3 to a greater degree than males.

## RESULTS

### Cochlear output is reduced in 5-week-old GluA3$^{KO}$ female mice raised in ambient sound but unaltered when raised in quiet

We performed a longitudinal study from P20 to P90 to determine the role of GluA3 in the hearing sensitivity of female mice. Statistical tests included two-way ANOVA for the comparisons of the click and pure tone thresholds and two-way mixed ANOVA followed by *post hoc* Holm- Šidák's for wave-1 amplitude and latency. First, GluA3$^{WT}$ and GluA3$^{KO}$ mice were raised to P20 in very low-level sound ("quiet," 10 dB SPL for mouse hearing; see STAR Methods; Figure 1A) compared to the normal vivarium ambient sound (40 dB SPL for mouse hearing). Data showed no difference between genotypes in ABR thresholds or wave-1 amplitudes at P20 (clicks $p = 0.10$, pure tones $p > 0.05$; wave-1 amplitude $p > 0.05$) (Table S1). After verifying the two groups of mice not being different at baseline, we split the mice into two groups: ambient and quiet up to P90, to see if the sound level made a difference in the hearing sensitivity in the absence of GluA3 (Figure 1A).

The first female mice group was raised in the same ambient sound levels (Figure 1B) as males.[6] See figure legend for $p$ values of clicks and pure tones thresholds and wave-1 amplitude. Our data show that postnatal day 35 (P35) female GluA3$^{KO}$ mice had significantly elevated pure tone thresholds at 12, 16, and 32 kHz (Figure 1B, top left; Table S2). Although there was an insignificant trend toward elevated response thresholds for the rest of the stimuli tested in response to clicks and 4, 8, and 24 kHz tones in the KO. In contrast to the male GluA3$^{KO}$ mice,[6] the female GluA3$^{KO}$ mice had significantly smaller click wave-1 amplitudes above 65 dB SPL (Figure 1B, bottom left; Table S2). To determine if reduced cochlear sensitivity in female GluA3$^{KO}$ persisted, we further tested the mice at 2 months (P60) and 3 months (P90) of age, with similar findings. At P60, ABRs show that mice raised in ambient sound levels have similar click thresholds between genotypes; however, the GluA3$^{KO}$ had elevated pure tone thresholds at 24 and 32 kHz, and reduced wave-1 amplitude above 50 dB SPL (Figure 1B, top and bottom center; Table S2). At P90, ABR thresholds were significantly elevated in female KO mice at 32 kHz only, and wave-1 amplitude was significantly reduced above 60 dB SPL (Figure 1B, top and bottom right; Table S2). The lack of significant threshold shifts at many frequencies at P90 despite the larger trends relative to P60 appeared to result from greater variance, potentially due to effects of the *Cdh23* age-related hearing loss phenotype in C57BL/6 mice. Wave-1 latency as a function of click level was similar between GluA3$^{KO}$ and GluA3$^{WT}$ at all ages tested (P20, P60, P90, $p > 0.05$; Table S2). Our findings show that lack of the AMPA receptor subunit GluA3 accelerates hearing loss of females raised in ambient sound levels.

Next, we aged the GluA3$^{WT}$ and GluA3$^{KO}$ mice up to three months in the quiet and performed ABRs at P35, P60, and P90 (Figure 1C). See figure legend for $p$ values of clicks and pure tones thresholds and wave-1 amplitude. In contrast to mice raised in the normal vivarium, there was no difference between genotypes in ABR click threshold, pure-tone thresholds, or click wave-1 amplitude at any age for mice raised in quiet (Figure 1C, top and bottom; Table S1). Wave-1 latency was also similar between the GluA3$^{WT}$ and GluA3$^{KO}$ mice at all ages tested (P20, P60, P90, $p > 0.05$; Table S1).

We next analyzed wave-1 amplitude as a function of stimulus level (input/output (I/O) slope; two-way ANOVA followed by *post hoc* Šidák's multiple comparison test; see figure legend for $p$ values) between the two genotypes from P20 to P90 in ambient and in quiet (Figure 1D). In ambient sound, we found that I/O slope at P35, P60, and P90 was significantly lower in GluA3$^{KO}$ than GluA3$^{WT}$ (Figure 1D, left). In contrast, we did not observe any difference in I/O slope between genotypes in quiet conditions (Figure 1D, right). As expected, I/O slope decreased with cochlear maturation and subsequent aging.[13–15] Interestingly, the largest reduction in I/O slope occurred for GluA3$^{KO}$ mice raised in ambient sound between P20 to P35 (Figure 1D), suggesting an ambient sound-evoked activity-dependent requirement for GluA3 during maturation of the cochlea. This effect on wave-1 amplitude suggests poor synchrony of action potential generation in the auditory nerve, potentially caused by synaptopathy in P35 GluA3$^{KO}$ female mice raised in ambient conditions.

### Ambient sound triggers hearing loss in female GluA3$^{KO}$ mice

As described previously, raising the mice in ambient sound levels from P20 to P90 elevated cochlear thresholds and reduced ABR wave-1 in the auditory nerve. Figure 2 compares ABR thresholds and wave-1 amplitudes for WT or KO in ambient vs. quiet conditions at P35, P60, and P90. Statistical tests included two-way ANOVA for the comparisons of the click and pure tone thresholds and two-way mixed ANOVA for wave-1 amplitude followed by *post hoc* Holm-Šidák's multiple comparison test at each age (see figure legend for $p$ values). In GluA3$^{WT}$ female mice we did not observe any differences in click and pure-tone thresholds, or wave-1 amplitudes when comparing mice raised in ambient sound to mice

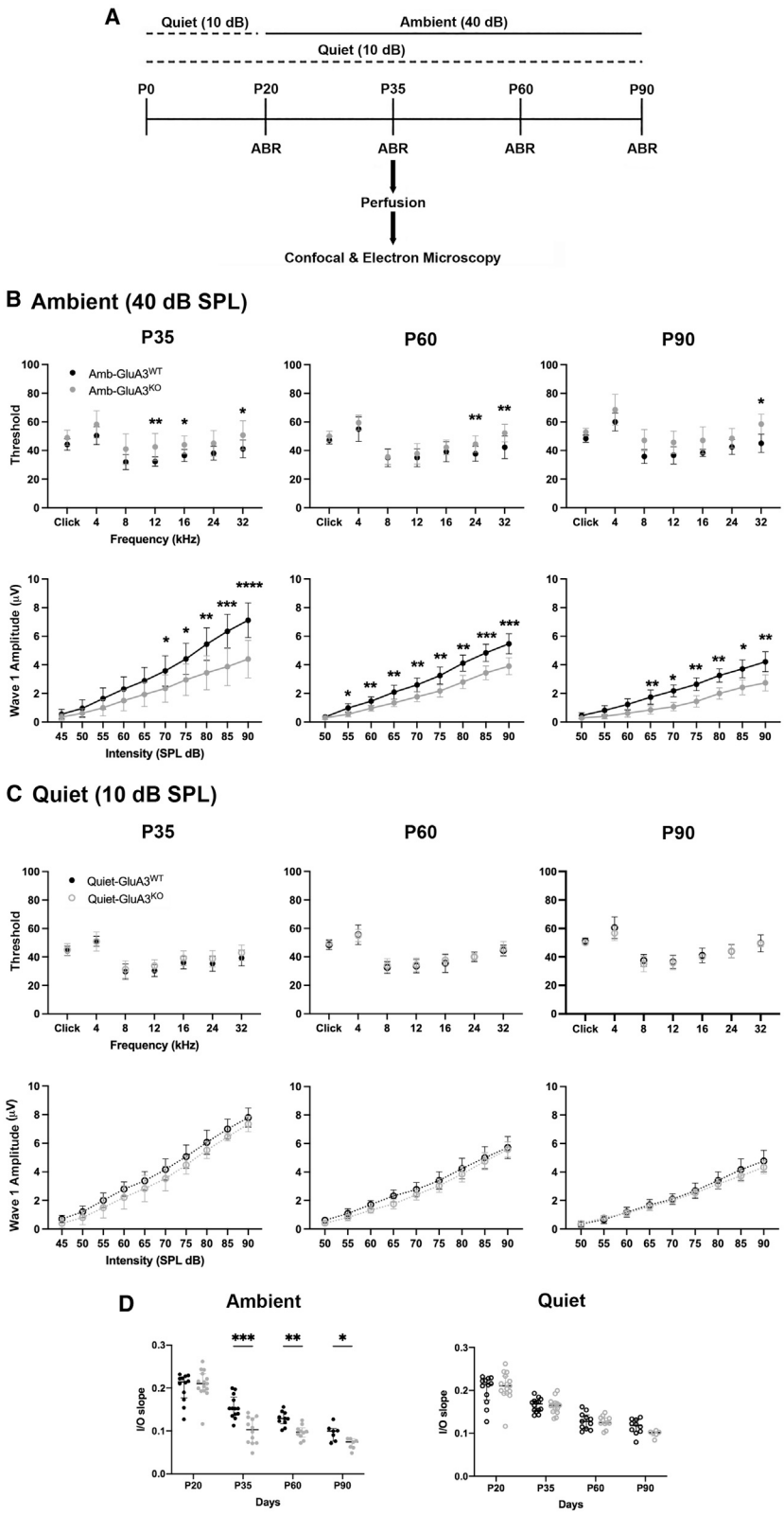


**Figure 1. ABR wave-I amplitude was reduced, and threshold was elevated in female mice raised in ambient sound**

(A) Summary of the experimental longitudinal design: ABRs were recorded at four different time points from the mice raised either in a facility with quiet sound conditions (10 dB SPL; dotted line) or ambient sound (40 dB SPL; solid line). At P35, some of the GluA3$^{WT}$ and GluA3$^{KO}$ mice ($n$ = 17) were transcardially perfused, and cochleae were collected for further ultrastructural and immunofluorescence, and confocal analyses.

(B) GluA3$^{WT}$ and GluA3$^{KO}$ mice raised in ambient sound levels. ABR data (mean ± SD); statistical tests included two-way ANOVA for the comparisons of the clicks and pure tone thresholds, and two-way mixed ANOVA followed by *post hoc* Holm- Šidák's for wave-1 amplitude. **P35** ($n$ = 13 GluA3$^{WT}$, $n$ = 14 GluA3$^{KO}$): click thresholds ($p$ = 0.10), pure tones thresholds ($p_{12kHz}$, $p_{16kHz}$ and $p_{32kHz}$ < 0.05; $p_{4kHz}$, $p_{8kHz}$ and $p_{24kHz}$ $p$ > 0.05), wave-1 amplitude above 65 dB SPL ($p$ < 0.05). **P60** ($n$ = 10 for each genotype): click thresholds ($p$ = 0.75), pure tones thresholds ($p_{4k\text{-}16\ kHz}$ > 0.05; $p_{24–32kHz}$ < 0.05) and wave-1 amplitude above 50 dB SPL ($p$ < 0.05). **P90** ($n$ = 10 for each genotype): click thresholds ($p$ = 0.07), pure tones thresholds ($p_{4k\text{-}24\ kHz}$ > 0.05, $p_{32\ kHz}$ < 0.05) and wave-1 amplitude above 60 dB SPL ($p$ < 0.05). Asterisks indicate the statistical differences (*$p$ < 0.05, **$p$ < 0.01, ***$p$ < 0.001, ****$p$ < 0.0001). See also Table S2.

(C) GluA3$^{WT}$ and GluA3$^{KO}$ mice reared in quiet sound levels. ABR data (mean ± SD), statistical tests included two-way ANOVA for the comparisons of the clicks and pure tone thresholds, and two-way mixed ANOVA followed by *post hoc* Holm- Šidák's for wave-1 amplitude. P35 ($n$ = 14 for each genotype), P60 ($n$ = 12 GluA3$^{WT}$, $n$ = 11 GluA3$^{KO}$), and P90 ($n$ = 12 GluA3$^{WT}$, $n$ = 6 GluA3$^{KO)}$: click thresholds ($p$ > 0.05), pure tones thresholds ($p_{8–32\ kHz}$ > 0.05), and wave-1 amplitude ($p$ > 0.05). See also Table S1.

(D) Input/output (I/O) slope of ABR wave-1 amplitude in GluA3$^{WT}$ and GluA3$^{KO}$ from P20 to P90 in ambient and quiet. two-way ANOVA followed by *post hoc* Šidák's multiple comparison test. In mice raised in ambient and relative to GluA3$^{WT}$ mice the I/O slope was significant at P35 ($p$ = 0.0004), at P60 ($p$ = 0.0018), and at P90 ($p$ = 0.045) (left). In mice raised in quiet the I/O slope was similar at all ages tested (P30, P60, and P90 $p$ > 0.05). Each data point shows individual ABR wave-I amplitude I/O slope as function of sound intensity. Data represents the median. Asterisks indicate the statistical differences (*$p$ < 0.05, **$p$ < 0.01, ***$p$ < 0.001). (P20, $n$ = 13 GluA3$^{WT}$, $n$ = 17 GluA3$^{KO}$; the number of mice for P30, P60, and P90 is as in Figures 1B and 1C).

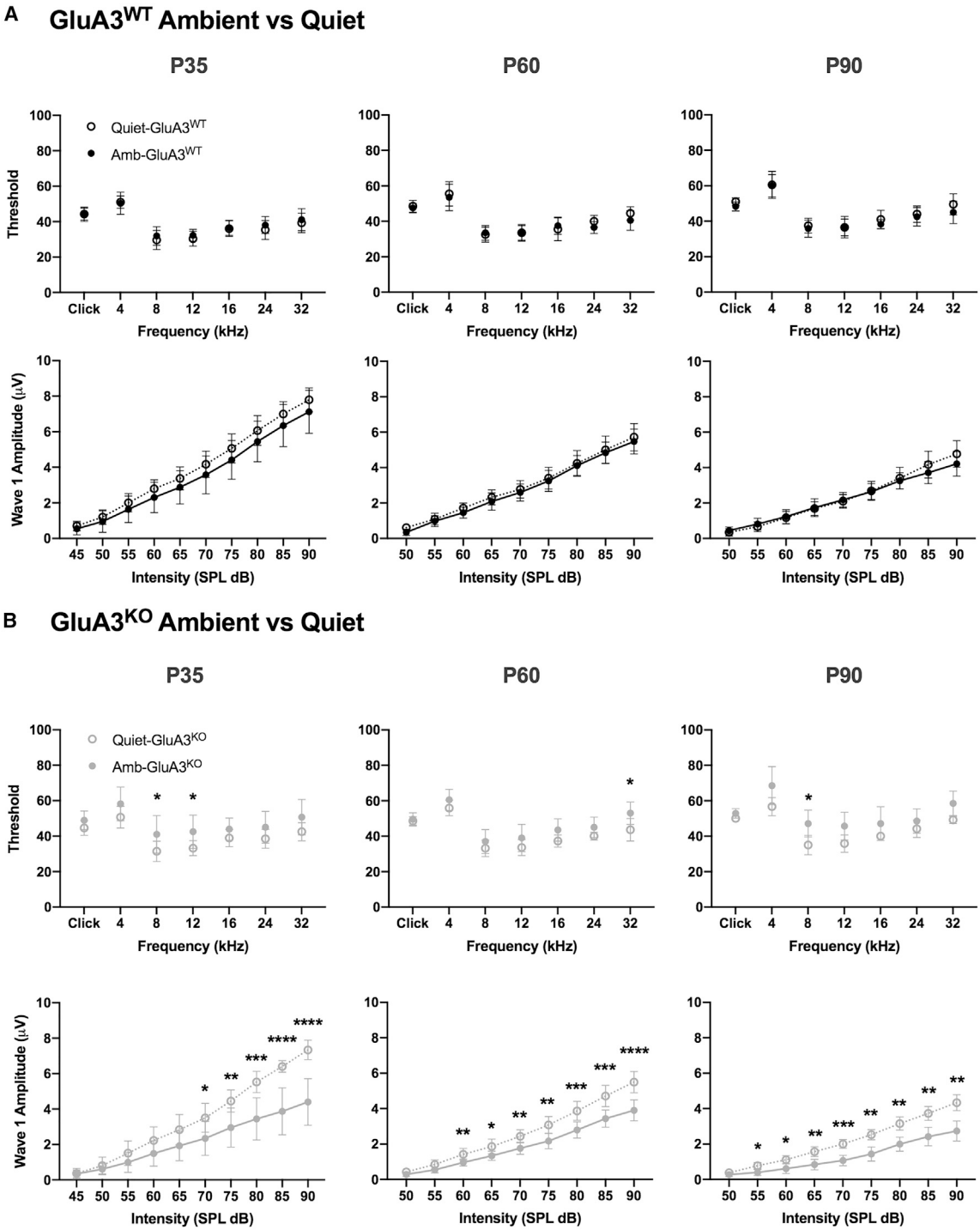


**Figure 2. Ambient sound triggers ABR click wave-I amplitude reduction in female GluA3$^{KO}$ mice**

(A and B) Statistical tests included two-way ANOVA for the comparisons of the click and pure tone thresholds and two-way mixed ANOVA for wave-1 amplitude followed by *post hoc* Holm-Sidák's multiple at each age. (A) GluA3$^{WT}$ mice raised in ambient and quiet show similar ABR clicks and pure tones thresholds (upper panel), and click wave-1 amplitude (lower panel) at P35, P60, and P90 (clicks $p > 0.05$, pure tones p $p_{4–32\ kHz} > 0.05$; wave-1 amplitude $p > 0.05$) for each of the age group). Data represented as mean ± SD. (B) GluA3$^{KO}$ mice raised in ambient and in quiet. ABR clicks and pure tones thresholds (upper panel), and click wave-I amplitude (lower panel) at P35, P60, and P90. **P35**: clicks thresholds ($p = 0.16$), pure tones thresholds ($p_{4\ kHz}$, $p_{16–32\ kHz} > 0.05$, $p_{8\ kHz} < 0.048$, $p_{12\ kHz} = 0.022$) and wave-1 amplitude above 65 dB SPL ($p < 0.05$ to 0.0001). **P60**: click thresholds ($p = 0.99$), pure tones thresholds ($p_{4–24\ kHz} > 0.05$, $p_{32\ kHz} = 0.022$) and wave-1 amplitude above 55 dB SPL ($p < 0.05$–0.0001). **P90**: click thresholds ($p = 0.19$), pure tones threshold ($p_{4\ kHz}$, $p_{12–32\ kHz} > 0.05$, $p_{8\ kHz} = 0.046$), and wave-1 amplitude ($p < 0.05$–0.001). Asterisks: *$p < 0.05$, **$p < 0.01$, ***$p < 0.001$, ****$p < 0.0001$. Data represented as mean ± SD. See also Tables S1 and S2.

raised in low-level (i.e., quiet) sound at any age (Figure 2A; Tables S1 and S2). In GluA3$^{KO}$ mice, click and pure-tone thresholds were similar at P35, except the 8 and 12 kHz pure tone thresholds that were significantly higher in the GluA3$^{KO}$ mice raised in ambient sound compared to those in quiet (Figure 2B; Tables S1 and S2). At P60 clicks and pure tone thresholds were similar in GluA3$^{KO}$ mice reared in ambient and in quiet except at 32 kHz thresholds that were higher in the KO mice raised in ambient. At P90, click thresholds were similar and the pure tone thresholds of the KO appeared to be higher in the ambient when compared to KO mice raised in quiet, but the difference was only statistically significant at 8 kHz (Figure 2B, upper). In contrast, wave-1 amplitude was significantly lower at all ages in GluA3$^{KO}$ mice raised in ambient compared to those in quiet. The reduction in wave-1 amplitude in the KO in ambient was found significant above 65 dB SPL at P35, above 55 dB SPL at P60, and above 50 dB SPL at P90 (Figure 2B, bottom).

In mice, the first postnatal month is a sensitive and critical period for the development of inner hair cell (IHC) ribbon synapses and cochlear function.[16–18] After the onset of hearing function at the end of the 2$^{nd}$ postnatal week, cochlear function continues to develop with the maturation of afferent axonal and synaptic anatomies.[17–20] Next, we asked if this reduction in wave-1 amplitude in female mice lacking GluA3 and raised in ambient sound was associated with cochlear synaptopathy: the pathological alteration, degradation, or loss of ribbon synapses.

## Ambient sound triggers synaptopathy in female GluA3$^{KO}$ mice

To assess cochlear synapses at 5 weeks of age (P35) with confocal microscopy, we immunolabeled the presynaptic ribbon and the postsynaptic AMPARs. Female GluA3$^{WT}$ and GluA3$^{KO}$ mice had similar numbers of paired synapses (juxtaposed pre- and post-synaptic markers) throughout the cochlea in both ambient and quiet conditions (Figure 3A, left and right; two-tailed Mann-Whitney U test with Holm- Šidák's correction for multiple comparisons for all tests in Figures 3 and 4; see legends for exact $p$ values $\geq$0.001). The number of paired synapses per IHC, mean across all images throughout the cochlea, was 15.3 and 15.5 for WT and KO, respectively, in ambient sound (for means by cochlear region, see Table S3). In quiet, the mean paired synapses per IHC were 17.3 in WT and 16.7 in KO. In contrast, the number of lone ribbons (anti-CtBP2 without juxtaposed postsynaptic markers) and the number of ribbonless synapses (anti-GluA2 and -GluA4 without juxtaposed CtBP2) per IHC were significantly greater throughout the cochlea in GluA3$^{KO}$ compared to WT, but only in ambient sound (Figures 3B and 3C, left; lone ribbons: mean of 0.83 in WT vs. 2.4 in KO; ribbonless: 0.90 vs. 2.4). In quiet conditions, GluA3$^{KO}$ had significantly fewer ribbonless synapses than WT in the 20 kHz region and when considering all regions as one (Figure 3C, right; mean of 1.1 in WT vs. 0.23 in KO), while lone ribbons in quiet were similar in WT and KO (Figure 3B, right; mean of 1.1 in WT vs. 0.8 in KO). Thus, relative to paired synapses ($\sim$15 per IHC), lone ribbons and ribbonless synapses were relatively rare in quiet and in WT in ambient sound ($\sim$0–2 per IHC, mean among images; group means of $\sim$1 per IHC). However, in GluA3$^{KO}$ raised in ambient sound, the group means were >2 per IHC (Figures 3B and 3C, left).

Some synapses (partially paired) contained a presynaptic ribbon juxtaposed to only GluA2 or, very rarely, only GluA4. In ambient sound, GluA3$^{KO}$ had significantly fewer GluA2-only synapses per IHC than WT throughout the cochlea (Figure 3D, left; mean of 1.2 in WT vs. 0.23 in KO; for means by cochlear region, see Table S3) and an insignificant trend toward a greater number of GluA4-only synapses than WT (Figure 3E, left; mean of 0.0 in WT vs. 0.042 in per IHC in KO). In quiet, both varieties of partially paired synapses were very rare: GluA2-only synapses were rarely seen in either genotype (Figure 3D, right; mean of 0.02 in WT vs. 0.06 per IHC in KO), while GluA4-only synapses were seen only in GluA3$^{KO}$ (Figure 3E, right; mean of 0 in WT vs. 0.07 per IHC in KO). Thus, GluA4-only synapses were seen only in GluA3$^{KO}$ for females in ambient or quiet conditions. Although GluA4-only synapses were significantly greater in number in male GluA3$^{KO}$ than WT raised in ambient conditions,[6] the differences did not reach statistical significance for the females (all synapses ambient, Figure 3E, left; all synapses quiet; Figure 3E, right).

Next, we focused on GluA2 and GluA4 intensity per synapse from females raised in ambient sound or quiet (Figure 4). Experiments were performed with GluA3$^{KO}$ and GluA3$^{WT}$ in parallel, separately for the two sound conditions, so comparisons are made only between GluA3$^{WT}$ and GluA3$^{KO}$. CtBP2 intensity did not differ by genotype in either condition ($p$ = 0.54 in ambient, $p$ = 0.10 in quiet; not shown). In Figures 4A and 4B, for visual clarity of GluA2 and GluA4, the CtBP2 fluorescence channel was replaced with a red marker at the centroid of each presynaptic ribbon, and white markers indicating ribbonless synapses. For GluA4 and GluA2 fluorescence intensity per synapse, in quiet conditions, the variance between images was relatively small, and the decrease in GluA2 intensity in the GluA3$^{KO}$ was significant (45% less than WT; $p$ = 0.001; not shown), while the decrease in GluA4 was not significant (16% less than WT; $p$ = 0.07; not shown. In ambient sound, we observed the same trends as in the males: an increase in GluA4 (70% more than WT; $p$ = 0.07; not shown) and a decrease in GluA2 in GluA3$^{KO}$ (17% less than WT; $p$ = 0.15; not shown), although these two trends did not reach statistical significance in ambient sound due to increased variance (Table S4). In Figures 4C and 4D, these data are displayed as means per image and per group after normalizing metrics from individual images to the respective WT mean for images from ambient or quiet conditions. Like the GluA3$^{KO}$ males raised in ambient sound,[6] in GluA3$^{KO}$ females the GluA4:GluA2 ratios were significantly increased in both quiet and ambient sound (103% increase in ambient vs. 56% increase in quiet; Figure 4E; $p$ < 0.001 for both). We next asked if synapses without a ribbon differed in GluA4:GluA2 ratio from synapses with a ribbon by comparing the ratios between those two groups of synapses within each image. Only in GluA3$^{WT}$ mice in ambient conditions, there was an obvious difference between ribbonless synapses and paired synapses, where the GluA4:GluA2 ratio was greater at ribbonless synapses than paired synapses (138% greater; Figure 4F; $p$ = 0.01). In ambient sound, the ribbonless-ratio/paired-ratio was significantly greater in WT than in KO by 99%.

At 5 weeks, the female GluA3$^{KO}$ mice raised in quiet had apparently normal ABR (Figures 1 and 2) and numbers of paired

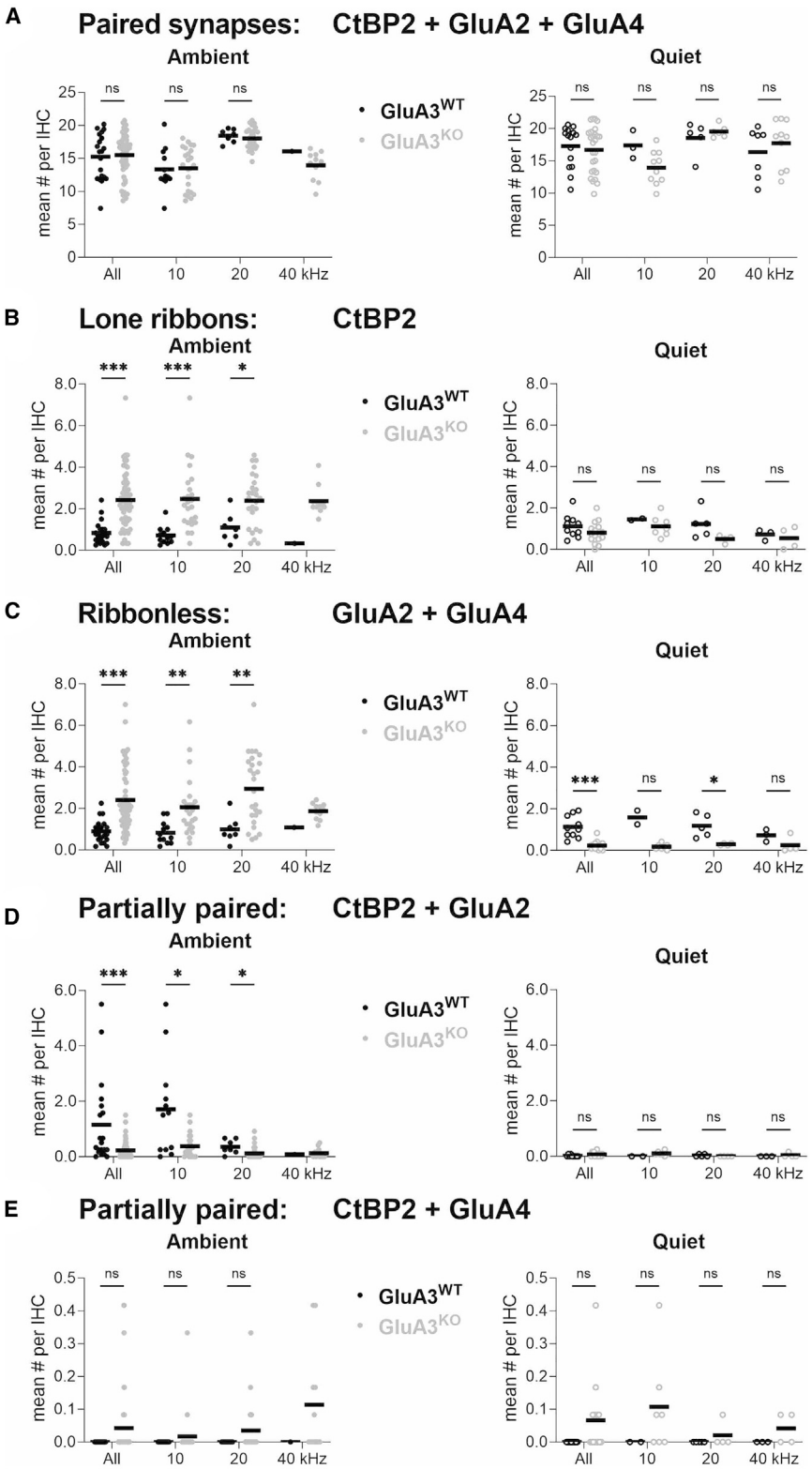


**Figure 3. Synapse counts for 5-week-old females raised in ambient sound or in quiet**

Number per inner hair cell for all synapses and divided into 3 tonotopic regions centered at 10, 20, or 40 kHz; GluA3$^{WT}$ (black), GluA3$^{KO}$ (gray); ambient (left, filled circles, $n$ = 20 WT and 61 KO images), quiet (right, open circles, $n$ = 15 WT and 26 KO images) from 4 WT to 5 KO mice. Markers are image means and bars are means of group means. Two-tailed Mann-Whitney U test with Holm- Šidák's correction for multiple comparisons; ns $p \geq 0.05$, $^{*}p < 0.05$, $^{**}p < 0.01$, $^{***}p < 0.001$. The lowest reported $p$ value is 0.001, so $p$ values lower than 0.001 are reported as $p < 0.001$.

(A) Paired synapses (CtBP2 + GluA2 + GluA4) were not significantly different in number between GluA3$^{WT}$ and GluA3$^{KO}$ for all synapses or in any of the 3 tonotopic regions in ambient sound or in quiet. Ambient: adjusted $p$ = 0.90, 0.90, and 0.89 for all synapses, 10 kHz, and 20 kHz regions, respectively; for the 40 kHz region $n$ = 1 image in WT precluded statistical comparison. Quiet: adjusted $p$ = 0.87, 0.27, 0.89, and 0.89 for all synapses, 10 kHz, 20 kHz, and 40 kHz regions, respectively.

(B) Lone ribbons (CtBP2 only) were significantly greater in number in GluA3$^{KO}$ than GluA3$^{WT}$ in ambient sound; not significantly different in quiet. Ambient: adjusted $p$ = < 0.001, < 0.001, and 0.02 for all synapses, 10 kHz, and 20 kHz regions, respectively; for the 40 kHz region $n$ = 1 image in WT precluded statistical comparison. Quiet: adjusted $p$ = 0.42, 0.44, 0.15, and 0.91 for all synapses, 10 kHz, 20 kHz, and 40 kHz regions, respectively.

(C) Ribbonless synapses (GluA2 + GluA4) were significantly greater in number in GluA3$^{KO}$ than GluA3$^{WT}$ in ambient sound; but significantly fewer in quiet. Ambient: adjusted $p$ = < 0.001, 0.001, and 0.005 for all synapses, 10 kHz, and 20 kHz regions, respectively; for the 40 kHz region $n$ = 1 image in WT precluded statistical comparison. Quiet: adjusted $p$ = < 0.001, 0.05, 0.04, and 0.17 for all synapses, 10 kHz, 20 kHz, and 40 kHz regions, respectively.

(D) Synapses lacking detectable GluA4 (CtBP2 + GluA2 only) were significantly fewer in number in GluA3$^{KO}$ than GluA3$^{WT}$ in ambient sound; not significantly different in quiet. Ambient: adjusted $p$ = < 0.001, 0.03, and 0.03 for all synapses, 10 kHz, and 20 kHz regions, respectively; for the 40 kHz region $n$ = 1 image in WT precluded statistical comparison. Quiet: adjusted $p$ = 0.42, 0.38, 0.69, and 0.99 for all synapses, 10 kHz, 20 kHz, and 40 kHz regions, respectively.

(E) Synapses lacking detectable GluA2 (CtBP2 + GluA4 only) were sometimes observed, only in GluA3$^{KO}$, but not significantly different in number in ambient sound or in quiet. Ambient: adjusted $p$ = 0.09, 0.54, and 0.51 for all synapses, 10 kHz, and 20 kHz regions, respectively; for the 40 kHz region $n$ = 1 image in WT precluded statistical comparison. Quiet: adjusted $p$ = 0.08, 0.80, 0.80, and 0.80 for all synapses, 10 kHz, 20 kHz, and 40 kHz regions, respectively. See also Table S3.

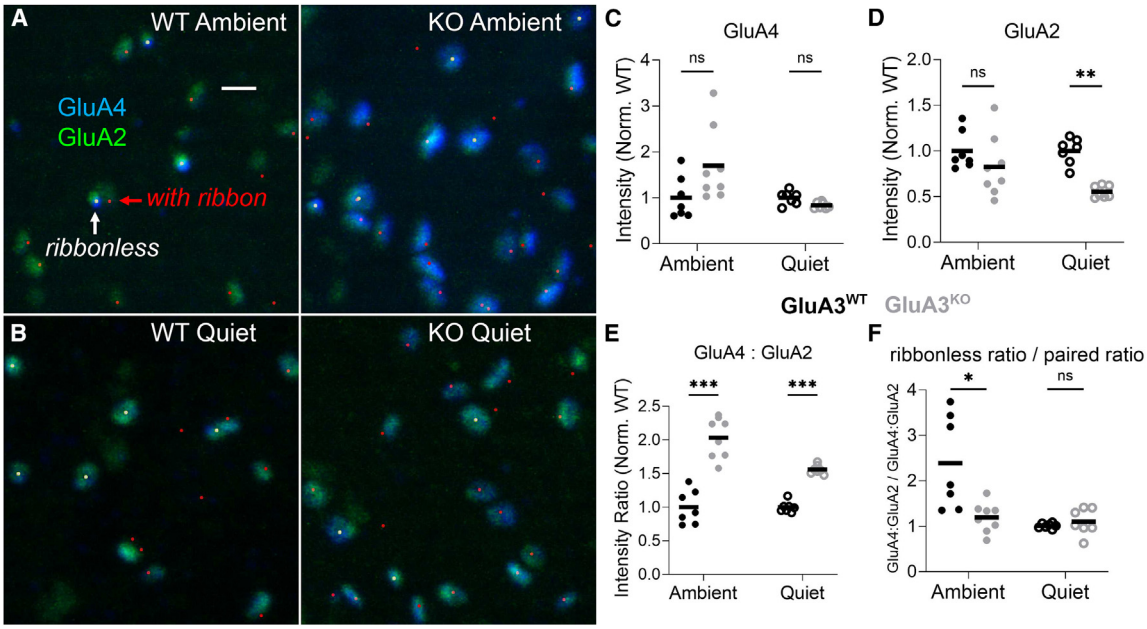


**Figure 4. AMPAR intensity analysis of synapses from 5-week-old females raised in ambient sound or quiet**

(A) Confocal images of anti-GluA2 (green) and anti-GluA4 (blue) for GluA3$^{WT}$ (left) and GluA3$^{KO}$ (right) raised in ambient sound. For visual clarity of the GluA labeling, the anti-CtBP2 fluorescence channel has been replaced with markers at the centroids of the presynaptic ribbons in the case of paired synapses (red dots). For ribbonless synapses, a white dot marks the center of the GluA cluster.

(B) Same as (A), for mice raised in quiet.

(C–F) GluA3$^{WT}$: black and GluA3$^{KO}$: gray.

(C) For GluA4 intensity per synapse, there was no significant difference between genotypes in ambient ($p$ = 0.07) or in quiet conditions ($p$ = 0.07).

(D) For GluA2 intensity per synapse, there was no significant difference between genotypes in ambient ($p$ = 0.15), but GluA3$^{WT}$ synapses had significantly more GluA2 fluorescence in quiet conditions ($p$ = 0.001).

(E) The GluA4:GluA2 intensity ratio per synapse was significantly greater for GluA3$^{KO}$ synapses in both ambient and in quiet conditions ($p$ = < 0.001).

(F) In each image, the mean GluA4:GluA2 intensity ratio for ribbonless synapses was divided by the mean GluA4:GluA2 intensity ratio for paired synapses, such that numbers greater than 1 indicate greater GluA4 fluorescence at ribbonless synapses than paired synapses. Ribbonless synapses had greater GluA4:GluA2 ratios than paired synapses for GluA3$^{WT}$ mice in ambient conditions ($p$ = 0.01) but they were similar in quiet ($p$ = 0.8). In (C–F), ambient (left, filled circles, $n$ = 7 WT and 7 KO images), quiet (right, open circles, $n$ = 7 WT and 7 KO images). Markers are image means and bars are means of group means. Two-tailed Mann-Whitney U test with Holm- Šidák's correction for multiple comparisons; ns $p \geq 0.05$, *$p < 0.05$, **$p < 0.01$, ***$p < 0.001$.

Image means were normalized to the WT group mean per sound condition in (C–E). See also Table S3.

synapses (Figure 3). Still, they had significantly reduced expression of GluA2 per synapse (Figure 4). Next, we looked within synapses for additional anatomical synaptopathy. Similar to a previous study,[21] we selected well-isolated synapses and divided each synapse into nanodomains to measure the GluA4:GluA2 fluorescence ratio (Figures 5A, 5B, and S1; see STAR Methods). In both genotypes, we observed a broad range of ratios within nanodomains, generally between ~0.1–2.0. However, in GluA3$^{KO}$, the ratios for whole synapses and nanodomains extended to greater values than in GluA3$^{WT}$, suggesting a greater fraction of AMPARs lacking the subunit GluA2 in GluA3$^{KO}$ (Figures 5C–5E). For whole synapses in WT: mean ratio 0.58 ± 0.13 (SD), range 0.29–0.95; in KO: mean ratio 0.76 ± 0.23, range 0.31–1.42. For nanodomains in WT: mean ratio 0.53 ± 0.24, range 0.099–1.77; in KO: mean ratio 0.70, range 0.12–2.8. Indeed, the probability distributions for synapses and nanodomains differed between GluA3$^{WT}$ and GluA3$^{KO}$ (KS test: synapses, $p$ = 7.2 e$^{-9}$; nanodomains, $p$ = 3.5 e$^{-19}$). The positive relationship between GluA4:GluA2 ratio and ribbon fluorescence per synapse is shown in Figure 5F, and the strength of the correlation was tested with Spearman's coefficient $r_s$. For GluA3$^{WT}$, the correlation was significant ($r_s$ 0.26 > critical value 0.18); for GluA3$^{KO}$, the correlation was not significant ($r_s$ 0.092 < critical value 0.18).

In the same set of synapses from female mice raised in quiet, we asked if the GluA4:GluA2 fluorescence ratios differed as a function of distance from the center of the synapse with radial distributions (Figures 6 and S1; see STAR Methods). Shells of pixel areas were created from concentric squares overlaid on maximum-intensity projections of Airyscan images in GluA3$^{WT}$ and KO (Figures 6A and 6B). For each fluorescence channel in each shell, the sum of pixel intensities was divided by the number of pixels to calculate shell density, and the GluA4:GluA2 density ratios were calculated for each shell in each synapse based on the raw values or the peak-normalized values (Figures 6C and 6D). Radial distributions of GluA4:GluA2 fluorescence ratio per synapse were grouped by genotype in 6 tonotopic regions (Figures 6E and 6F). This analysis confirmed the observation of greater GluA4:GluA2 fluorescence ratios in GluA3$^{KO}$ relative to WT and shows this to be the case throughout intrasynaptic

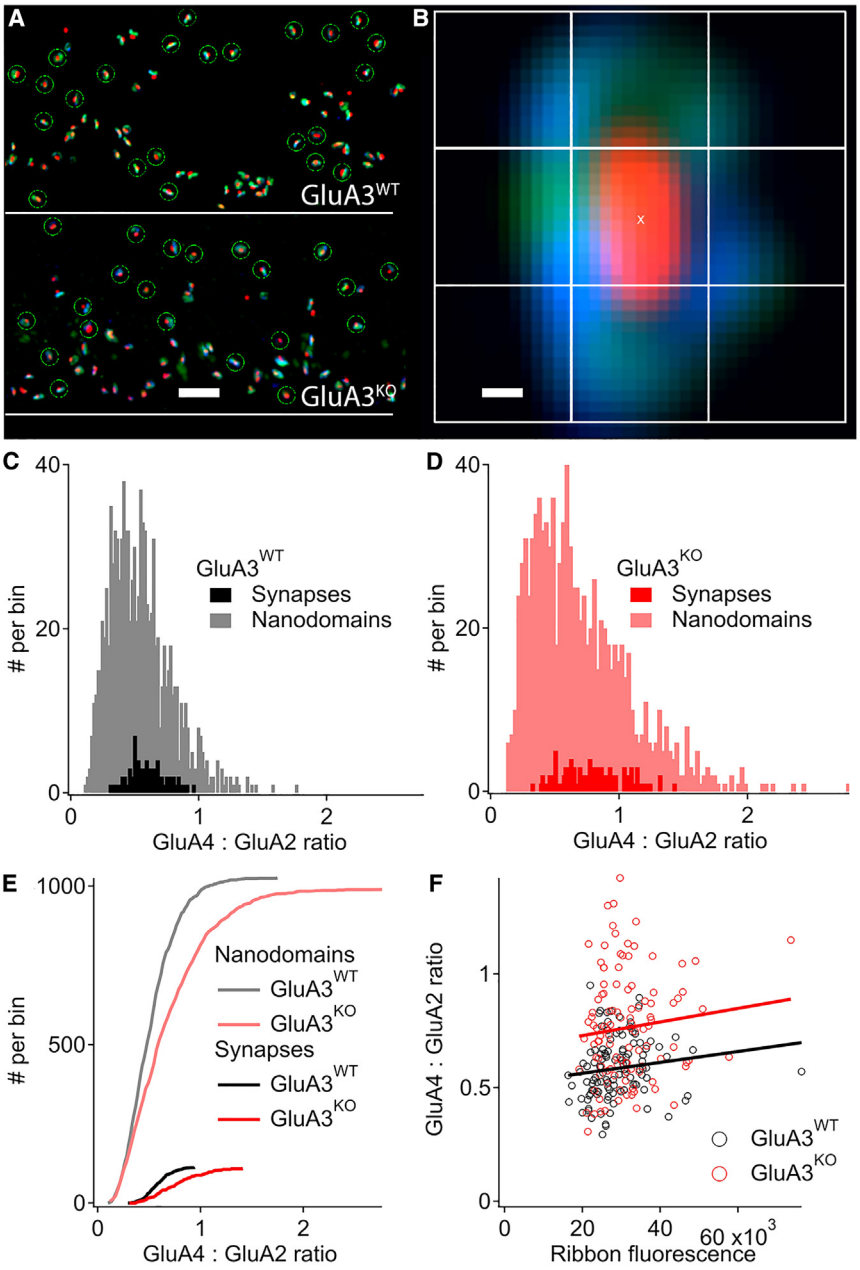


**Figure 5. AMPA receptor subunit fluorescence ratios in whole synapses and nanodomains from 5-week-old female mice raised in quiet**

(A) GluA3$^{WT}$ (upper) and GluA3$^{KO}$ (lower) synapses on inner hair cells in the 38 kHz tonotopic region labeled with anti-CtBP2 (red), anti-GluA4 (blue), and anti-GluA2 (green).

(B) Individual synapse with 9 square 13×13 pixel matrices overlaid for nanodomain analysis. Each pixel is 26 nm.

(C and D) Frequency histograms of ratios of raw GluA4:GluA2 fluorescence for whole synapses (black, dark red) and nanodomains (gray, light red) for GluA3$^{WT}$ (C) and GluA3$^{KO}$ (D). Data from mid-cochlea. WT: 1,026 nanodomains in 114 synapses from 4 images; KO: 990 nanodomains in 110 synapses from 4 images.

(E) Cumulative histograms of the data in (C) and (D). Comparing genotypes, the distributions of ratios were significantly different for synapses (KS test, $p$ = 7.2 e$^{-9}$) and for nanodomains within synapses (nanodomains, $p$ = 3.5 e$^{-19}$).

(F) GluA4:GluA2 fluorescence ratios per synapse as a function of ribbon fluorescence. The variables were significantly correlated for GluA3$^{WT}$ ($r_s$ 0.26 > critical value 0.18) but not for GluA3$^{KO}$ ($r_s$ 0.092 < critical value 0.18).

Scale bars: (A) 2 μm; (B) 100 nm. See also Figure S1 and Table S3.

space when comparing similar tonotopic regions. On average, ratios tended to peak 200–400 nm from the synapse center in both genotypes, but this peak was less pronounced in GluA3$^{KO}$ because GluA4:GluA2 ratios tended to be greater near the synapse center in GluA3$^{KO}$ relative to GluA3$^{WT}$. Thus, it appears that lack of GluA3 alters the intrasynaptic distribution of GluA2 and GluA4.

## Afferent swellings in the 5-week-old female GluA3$^{KO}$ in ambient

To look for structural correlates of hearing impairment in the GluA3-deficient cochlea, we analyzed ultrastructurally the sensory epithelium of the mice raised in ambient and quiet sound conditions. The general structure and cellular components of the sensory epithelium of the female GluA3$^{KO}$ raised in ambient and quiet were similar to GluA3$^{WT}$ and published data of C57BL/6 mice.[22] However, in the P35 female KO raised in ambient conditions, we noticed the existence of vacuoles underneath IHCs, which were most often observed in the high to middle frequency, basal-middle part of the cochlear spiral (Figures 7D, 7F, 7G, and S2). We confirmed that the vacuoles corresponded to swellings of type I afferent terminals synapsing on both sides of the IHCs (modiolar and pillar, Figures 7F, 7G, and S2). Relative to other parts of the neuronal cytoplasm, these vacuoles were clearer, suggesting less density of electron-absorbing intracellular material. Some afferent swellings had a post-synaptic density (PSD) juxtaposed with a membrane-anchored pre-synaptic ribbon (Figure 7F), whereas others were ribbonless (Figure 7G). The cytoplasm of the swollen afferents showed missing mitochondria and swollen endoplasmic reticulum. Alongside the swollen afferents, normal-looking afferent terminals with electron-dense PSDs and membrane-anchored presynaptic ribbons were present (Figure 7E). We calculated the average gray value (AGV) of the cytoplasm of the afferent terminals and found that in the GluA3$^{KO}$ the cytoplasm of the

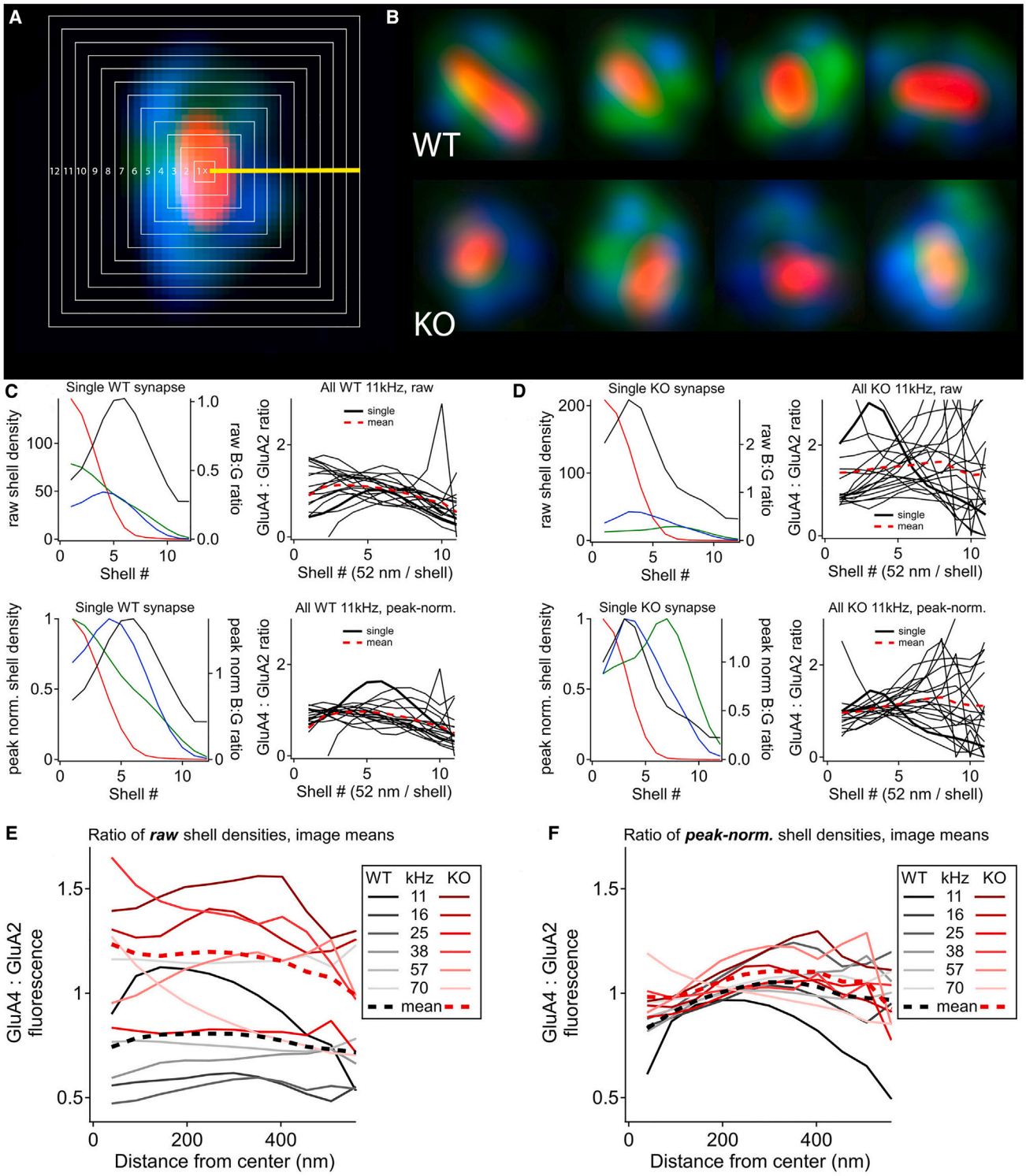


**Figure 6. Radial distribution of AMPA receptors around synapse center in 5-week-old female mice raised in quiet**

(A) Squares were overlaid on synapses in 2-dimensional maximum-intensity projections to create shells for calculation of 1-dimensional radial distributions of blue to green fluorescence density to approximate changes in the relative abundance of GluA4:GluA2 as a function of distance from ribbon center.

(B) Examples of synapses from GluA3$^{WT}$ (upper) and GluA3$^{KO}$ (lower).

(C) Upper left: radial distribution of raw shell densities for the WT synapse in (A) for CtBP2 (red), GluA4 (blue), and GluA2 (green). In black is the ratio of raw blue to green fluorescence. Upper right: ratio of raw GluA4:GluA2 shell densities for the WT synapses from the image of the 11 kHz region; single synapse on the left is

*(legend continued on next page)*

swollen afferents (AGV mean = 150 ± 23.4 ±SD; AGV scale settings black = 0 and white = 255) was significantly lighter than the "normal-looking" afferents in the KO (AGV mean = 105 ± 20.2 ±SD) or the GluA3$^{WT}$ afferents (AGV mean = 102 ± 11.6 ±SD) ($p < 0.0001$, one-way ANOVA). A paired comparison between the AGV of the WT afferents and the "normal-looking" afferents in the GluA3$^{KO}$ showed no difference ($p > 0.005$). In addition, we found that the swollen afferents in GluA3$^{KO}$ (circularity mean = 0.8 ± 0.1 ± SD; roundness mean = 0.74 ± 0.13 ±SD) were significantly more circular and rounder than the "normal-looking" afferents in the KO (circularity mean = 0.6 ± 0.11 ± SD; roundness mean = 0.44 ± 0.15 ±SD) or the GluA3$^{WT}$ afferents (circularity mean = 0.43 ± 0.1 ± SD; roundness mean = 0.41 ± 0.17 ±SD) ($p < 0.0001$, one-way ANOVA). A paired comparison between the "normal-looking" afferents in the KO and the GluA3$^{WT}$ afferents showed that the formers were more circular ($p = 0.045$). In this analysis, we did not separate the data between modiolar and pillar side synapses. The observation of vacuole-associated type I afferent swellings increased in the female KO at P60 (Figure S2) and were also observed in the apex of the cochlear spiral. Swelling of afferent terminals suggests glutamate excitotoxicity and synaptophathy in GluA3$^{KO}$, reminiscent of noise-exposed or ischemic tissue from animals with intact GluA3.[23–25] Vacuoles or afferent swellings were not observed in female GluA3$^{WT}$ mice in ambient or in either genotype raised in quiet, in which only normal-looking synapses were observed (Figures 7A–7C and 7H–7K). Our results show chronic synaptopathy appearing ultra-structurally and physiologically before potential deafferentation of the IHC in female GluA3$^{KO}$ mice raised in ambient sound.

## Pre- and post-synaptic ultrastructural features of IHC-ribbon synapses in 5-week-old female mice raised in quiet

Previously, we reported that P35 male GluA3$^{KO}$ mice raised in ambient sound levels had normal ABR and a similar number of paired IHC-ribbon synapses. However, those male KO mice showed defective differentiation of modiolar-side and pillar-side pre- and post-synaptic ultrastructural specializations.[6] Due to the abundance of swollen afferents in the female GluA3$^{KO}$ in ambient, we performed morphometric analysis of the pre- and post-synaptic structure of the modiolar- and pillar-side IHC-ribbon synapses in 5-week GluA3$^{WT}$ and GluA3$^{KO}$ mice raised in quiet. This analysis of synapses from mice raised in quiet allows us to determine structural alterations associated with increased synaptic vulnerability in louder sound environments.

### *Ultrastructure in C57BL/6 GluA3$^{WT}$ in quiet*

Thirty-five IHC-ribbon synapses of female GluA3$^{WT}$ mice were analyzed in three dimensions (3D) using ultrathin serial sections (on average, 10 ultrathin sections per PSD). Of this total, 24 synapses were on the modiolar side and 11 on the pillar side of IHCs. In our sample of modiolar-side synapses, 19 had one single ribbon, whereas 5 had two ribbons. All pillar-side synapses had only one ribbon. We did not find differences in PSD surface area or volume between the modiolar synapses with one or two ribbons, so data were combined. Next, we compared the PSD surface area and volume between modiolar side and pillar side and did not observe any difference in GluA3$^{WT}$ (surface area $p = 0.52$; volume $p = 0.10$, unpaired t test) (Figure 8A, top; Table 1). In contrast, male GluA3$^{WT}$ PSDs were larger on the modiolar side.[6] Data from single ultrathin sections showed that the PSD linear length was similar between the modiolar- and pillar-side synapses ($p = 0.93$, Mann-Whitney test) (Figure 8B, top; Table 2).

We next compared the presynaptic ribbon surface area and volume between modiolar- and pillar-side synapses in GluA3$^{WT}$ (Figure 8A, top; Table 1). The ribbon surface area of the modiolar-side was significantly larger than the pillar-side ($p = 0.03$, unpaired t test). In contrast, ribbon volume was similar ($p = 0.56$).

Analysis of the presynaptic ribbon major and minor axes (unpaired t test) showed that the major axis of modiolar-side ribbons was not significantly different from the pillar side ($p = 0.06$) (Figure 8B, top; Table 2), in contrast to GluA3$^{WT}$ males.[6] The minor axis of modiolar-side ribbons was significantly smaller than the pillar side ($p = <0.0001$) (Figure 8B, top; Table 2). Moreover, ribbons of the modiolar-side were less circular ($p = 0.0002$, unpaired t test) and more elliptical ($p = 0.0001$, unpaired t test) than those on the pillar side (Figure 8B, top; Table 2), as was observed in the males. Analysis of synaptic vesicles (SVs) showed that those of the modiolar-side were larger than those of the pillar-side ($p = 0.0005$, Mann-Whitney test) (Figure 8B, top; Table 2), as in the males.[6]

### *Ultrastructure in C57BL/6 GluA3$^{KO}$ in quiet*

From GluA3$^{KO}$, 35 IHC-ribbon synapses were analyzed in 3D with serial ultrathin sections (on average, 10 ultrathin sections per PSD). Of this total, 24 were on the modiolar side and 11 on the pillar side of the IHCs. Seventeen synapses on the modiolar-side had one ribbon, whereas 7 had double ribbons. In contrast to GluA3$^{WT}$, 3 synapses on the pillar-side in GluA3$^{KO}$ mice had 2 ribbons, whereas 8 had a single ribbon. We did not find differences in PSD surface area or volume between the modiolar or pillar synapses with one or two ribbons, so data were combined. We then compared the PSD surface area and volume between the modiolar and pillar sides. All statistical tests in Figure 8 are unpaired t test unless noted. Similar to the GluA3$^{WT}$, there was no significant difference in the PSD surface area ($p = 0.16$) or volume ($p = 0.31$) (Figure 8A, bottom; Table 1). Unlike the GluA3$^{WT}$, the PSD length was significantly greater on the modiolar than on the pillar side ($p = 0.028$, Mann-Whitney test) (Figure 8B, bottom; Table 2).

The analysis of presynaptic ribbon surface area showed that those on the modiolar side had significantly larger surface area

shown in thick black trace; the image mean is shown in the dashed red trace. Lower left: radial distribution for the same synapse when normalized to the peak shell density of each fluorescence channel. Lower right: ratio of peak-normalized GluA4:GluA2 shell densities for the same image.

(D) Same as (C) for the KO image from the 11 kHz region.

(E) Image means of the ratio of raw shell densities for WT and KO. Group means are in thick dashed lines for WT (black) and KO (red).

(F) Same as (E) for the ratio of peak-normalized shell densities. See also Figure S1 and Table S3.

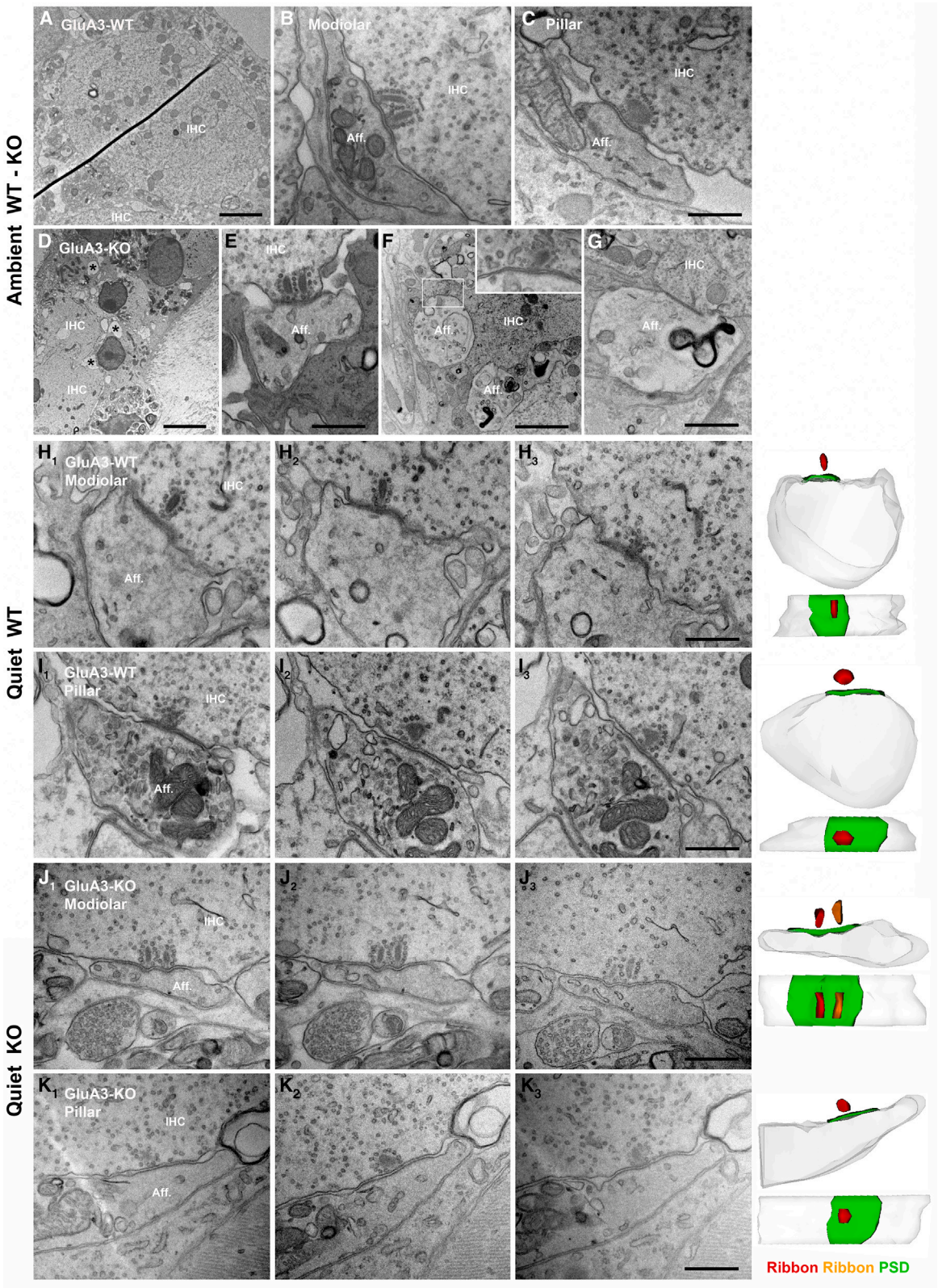


*(legend on next page)*

than those on the pillar side ($p = 0.007$) (Figure 8A, bottom; Table 1). In contrast, ribbon volume was similar between the modiolar and pillar sides ($p = 0.12$) (Figure 8A, bottom; Table 1).

Like GluA3$^{WT}$ females, the major axis of the KO, was similar between the modiolar- and pillar-side ribbons ($p = 0.08$) (Figure 8B, bottom; Table 2). In contrast to GluA3$^{WT}$ mice, the minor axis of the KO, was similar between the ribbons of the modiolar- and pillar-side synapses ($p = 0.15$) (Figure 8B, bottom; Table 2). Pillar-side ribbons were more circular ($p = 0.001$) and round ($p = 0.005$) than modiolar-side ribbons (Figure 8B, bottom; Table 2), but the difference was less significant than in the GluA3$^{WT}$. The analysis of the SVs size on modiolar- and pillar-side synapses showed that they were similar ($p = 0.63$, Mann-Whitney test) (Figure 8B; Table 2).

## SV size and ribbon shape were altered in the 5-week-old female GluA3$^{KO}$ mice in quiet

Next, we compared the pre- and post-synaptic ultrastructural features on the modiolar- and pillar-side synapses between genotypes (unpaired t test in all the comparisons). The PSD surface area and volume were similar on the modiolar (surface area $p = 0.43$; volume $p = 0.16$) and pillar side synapses (surface area $p = 0.78$; volume $p = 0.74$) between GluA3$^{KO}$ and GluA3$^{WT}$ mice (Figure 9A, left). No differences in PSD length were observed between genotypes (modiolar $p = 0.68$; pillar $p = 0.11$) (Figure 9B, top left).

Synaptic ribbon surface area on the modiolar side was significantly reduced in GluA3$^{KO}$ compared to GluA3$^{WT}$ ($p = 0.0096$). In comparison, the surface area on the pillar side was similar between the genotypes ($p = 0.073$) (Figure 9A, right). Ribbon volumes on the modiolar side were similar between GluA3$^{KO}$ and GluA3$^{WT}$ ($p = 0.25$), whereas, on the pillar side, the ribbon volumes of GluA3$^{KO}$ were significantly smaller than GluA3$^{WT}$ ($p = 0.029$) (Figure 9A, right). There was no significant difference in ribbon major axes on the modiolar- or pillar-side synapses between the GluA3$^{WT}$ and GluA3$^{KO}$ (modiolar: $p = 0.34$, pillar: $p = 0.56$). In contrast, the ribbon minor axes of GluA3$^{KO}$ modiolar side synapses were larger than those of the GluA3$^{WT}$ ($p = 0.018$). The minor axes of pillar side synapses were the same between genotypes ($p = 0.12$) (Figure 9B, center). The ribbon of modiolar side synapses of GluA3$^{KO}$ was more circular and rounder than in GluA3$^{WT}$ (circularity, $p = 0.049$, roundness, $p = 0.010$). On pillar-side synapses, ribbon circularity and roundness were similar between the genotypes (circularity, $p = 0.90$, roundness, $p = 0.36$) (Figure 9B, bottom). While SV size on the modiolar side was similar between genotypes, those on the pillar side were significantly larger in GluA3$^{KO}$ mice (modiolar, $p = 0.059$, pillar, $p < 0.0001$) (Figure 9B, top right).

Next, we designed an analysis in 2D to determine the ribbon shape by dividing the major to the minor axis (see STAR Methods); this ratio is independent of size. The schematic diagram in Figure 9C explains that round ribbons (shown in dark purple) have equal lengths on the major and minor axes. In contrast, elliptical ribbons (shown in red) have a major axis longer than the minor. The pie charts show the variability in ribbon shape from round to elongated as a total (modiolar + pillar) and then separated by modiolar- and pillar-side ribbons (Figure 9C). Overall, ribbons in GluA3$^{WT}$ and GluA3$^{KO}$ varied in shape from round to elongated; however, the KO ribbons were less elongated and rounder (Figure 9C, top pie chart). When comparing the shapes separated by modiolar and pillar, data showed that 18% of the modiolar-side ribbons in the GluA3$^{WT}$ mice were elliptical, although a larger percentage (36%) were round. In the WT pillar-side ribbons, the large majority (60%) was round, and the elliptical ribbons were not observed (Figure 9C). In the GluA3$^{KO}$, in contrast to the GluA3$^{WT}$, we did not find the most elliptical category within the modiolar-side ribbons. In the KO, 15% of modiolar ribbons were round and the rest (85%) were between elliptical and round. Almost half (47%) of pillar-side ribbons in the GluA3$^{KO}$ were round and the others had intermediary shapes (Figure 9C).

In summary, our ultrastructural data from 5-week-old female mice raised in quiet showed that in contrast to the GluA3$^{WT}$, the PSD length of the GluA3$^{KO}$ modiolar and pillar side synapses differed (smaller in the pillar). However, this difference was not significant when compared between genotypes. In addition, we observed that the shape of the pre-synaptic ribbons of both synapse types and the SV size of pillar-side synapses were altered in the female GluA3$^{KO}$ mice in quiet.

## Type I afferent terminals in the GluA3$^{KO}$ mice in quiet had a decrease in mitochondria content

Mitochondria often occupy neurons and have many protective properties, including their role in calcium buffering.[26–28] To

**Figure 7. Pre- and post-synaptic ultrastructural features of IHC-ribbon synapses of 5-week-old female GluA3$^{WT}$ and GluA3$^{KO}$ mice**

(A–C) Representative transmission electron microscopy (TEM) micrographs of IHC-ribbon synapses of GluA3$^{WT}$ mice ($n = 2$) raised in ambient sound. Micrographs are from the middle cochlea turn. (A) The micrograph shows a low magnification of one inner hair cell (IHC) in cross-section. Scale bar: 2 μm. (B and C) Micrographs show one modiolar (B) and one pillar (C) side IHC-ribbon synapse. The modiolar-side synapse has two presynaptic ribbons. Scale bar: 0.5 μm. Aff., afferent.

(D–G) Representative TEM micrographs of IHC-ribbon synapses of GluA3$^{KO}$ mice ($n = 2$) raised ambient sound. Micrographs are from the middle cochlea turn. (D) TEM micrograph showing afferent swellings (asterisks) around IHCs. Scale bar: 5 μm. (E) The micrograph shows a normal-looking double-ribbon modiolar IHC-ribbon synapse, Scale bar: 0.5 μm. (F) Micrograph shows afferent terminal swellings synapsing on an IHC. Scale bar: 2 μm. The inset shows a higher magnification of the white box region. The insets show details of pre- and post-synaptic membranes with the adjacent presynaptic ribbon. (G) Micrograph shows one afferent swelling with a flat postsynaptic membrane but without a pre-synaptic ribbon. Scale bar: 0.5 μm

($H_1$–$I_3$) Representative TEM serial electron micrographs of one IHC-ribbon synapse on the modiolar side ($H_1$–$H_3$) and on the pillar side ($I_1$–$I_3$) with their corresponding 3D reconstructions (right side) and its 3D reconstruction (right side) of GluA3$^{WT}$ mice raised in quiet. Micrographs are from the middle cochlea turn. Scale bar: 0.5 μm

($J_1$–$K_3$) Representative TEM serial electron micrographs of one IHC-ribbon synapse on the modiolar side ($J_1$–$J_3$) and the pillar side ($K_1$–$K_3$) with their corresponding 3D reconstructions (right side) of GluA3$^{KO}$ mice raised in quiet. No afferent swellings are observed in the GluA3$^{KO}$ in the quiet. Micrographs are from the middle cochlea turn. Scale bar: 0.5 μm. See also Figure S2.

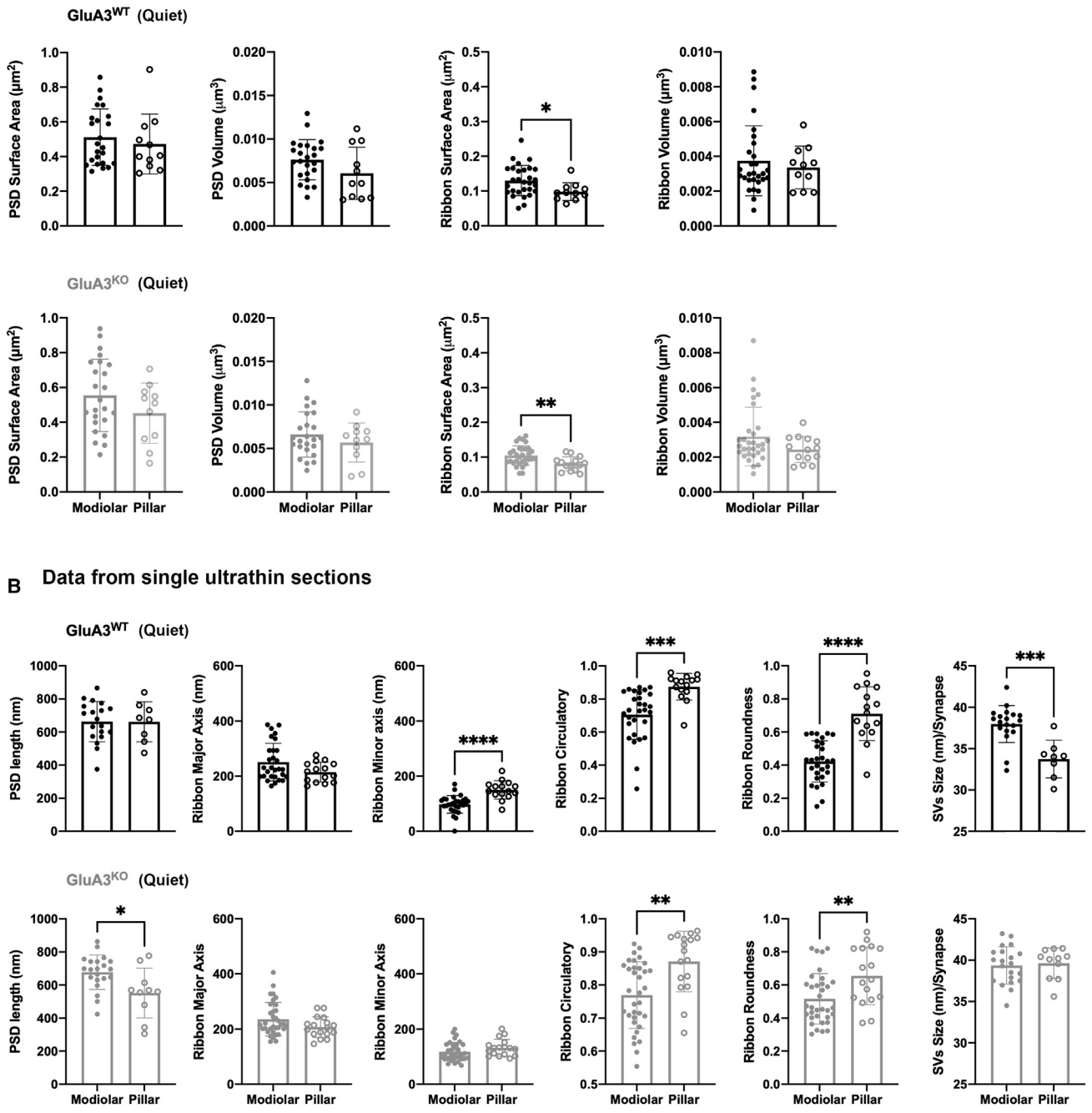


**Figure 8. Morphometric analysis of mid-cochlear IHC-ribbon synapses of P35 GluA3$^{WT}$ and GluA3$^{KO}$ mice in quiet**

(A) Plots of the quantitative data from 3D reconstructions of the PSD and ribbon surface area and volume of GluA3$^{WT}$ (black, upper panel) and GluA3$^{KO}$ mice (gray, lower panel). Data represented as mean ± SD, unpaired t test, *$p$ < 0.05, **$p$ < 0.01; $n$ = 35 synapses per genotype. See Table 1 for descriptive analysis.

(B) Plots of the quantitative data from single ultrathin sections of the PSD length, ribbon major and minor axis, ribbon circularity and roundness, and synaptic vesicles size (SVs) of IHC-ribbon synapses of GluA3$^{WT}$ (black, upper panel) and GluA3$^{KO}$ (gray, lower panel). Data represented as mean ± SD, unpaired t test, *$p$ < 0.05, **$p$ < 0.01, Mann-Whitney test; Synapses $n$ = 62 GluA3$^{WT}$, $n$ = 66 GluA3$^{KO}$. See Table 2 for descriptive analysis.

analyze the presence of mitochondria in the afferent terminals of Type I SGNs on IHCs, we quantified the number and percentage of mitochondria in modiolar- and pillar-side afferents of GluA3$^{WT}$ and GluA3$^{KO}$ mice in quiet (Figure 9D, left). In GluA3$^{WT}$, out of the total afferent terminals analyzed along modiolar and pillar side of hair cells, 20% of modiolar-side afferent terminals were without

**Table 1. Data from 3D reconstructions of IHC-ribbon synapses from mice raised in quiet**

| | | PSD surface area ($\mu m^2$) | | PSD volume ($\mu m^3$) | | Ribbon surface area ($\mu m^2$) | | Ribbon volume ($\mu m^3$) | |
|---|---|---|---|---|---|---|---|---|---|
| Genotypes | Parameters | M | P | M | P | M | P | M | P |
| $GluA3^{WT}$ | Minimum | 0.32 | 0.30 | 0.003 | 0.003 | 0.05 | 0.06 | 0.001 | 0.002 |
| | 25% Percentile | 0.36 | 0.35 | 0.006 | 0.003 | 0.10 | 0.08 | 0.003 | 0.002 |
| | Median | 0.46 | 0.41 | 0.008 | 0.005 | 0.13 | 0.09 | 0.003 | 0.004 |
| | 75% Percentile | 0.63 | 0.57 | 0.009 | 0.010 | 0.16 | 0.11 | 0.004 | 0.004 |
| | Maximum | 0.86 | 0.90 | 0.013 | 0.011 | 0.25 | 0.16 | 0.009 | 0.006 |
| | Mean | 0.51 | 0.47 | 0.008 | 0.006 | 0.13 | 0.10 | 0.004 | 0.003 |
| | Std. Deviation | 0.16 | 0.17 | 0.002 | 0.003 | 0.04 | 0.03 | 0.002 | 0.001 |
| | Coefficient of variation | 32% | 37% | 30% | 50% | 34% | 26% | 54% | 36% |
| $GluA3^{KO}$ | Minimum | 0.21 | 0.16 | 0.002 | 0.002 | 0.05 | 0.05 | 0.001 | 0.001 |
| | 25% Percentile | 0.40 | 0.31 | 0.005 | 0.004 | 0.09 | 0.06 | 0.002 | 0.002 |
| | Median | 0.50 | 0.51 | 0.006 | 0.006 | 0.10 | 0.08 | 0.003 | 0.002 |
| | 75% Percentile | 0.74 | 0.58 | 0.009 | 0.007 | 0.12 | 0.09 | 0.004 | 0.003 |
| | Maximum | 0.94 | 0.71 | 0.013 | 0.009 | 0.16 | 0.12 | 0.009 | 0.004 |
| | Mean | 0.55 | 0.45 | 0.007 | 0.006 | 0.10 | 0.08 | 0.003 | 0.002 |
| | Std. Deviation | 0.21 | 0.17 | 0.003 | 0.002 | 0.03 | 0.02 | 0.002 | 0.001 |
| | Coefficient of variation | 38% | 38% | 40% | 40% | 27% | 25% | 53% | 31% |

M, modiolar; P, pillar.

mitochondria, whereas 43% had (range: 1–9 mitochondria per afferent; median: 3). In contrast, all the pillar-side afferent terminals (representing 37% of the total) had mitochondria (range: 1–8 mitochondria per afferent; median: 4). The analysis of the $GluA3^{KO}$ shows that out of the total, 26% of the modiolar-side afferents lacked mitochondria, whereas most had them (42% of the total; range: 1–8 mitochondria per afferent; median: 2). Of the pillar-side afferents, we found that in contrast to the $GluA3^{WT}$, 7% lacked mitochondria whereas 25% had them (range: 1–8 mitochondria per afferent; median: 4). Overall, we find that in $GluA3^{KO}$ mice, there is an increase in the percentage of both modiolar- and pillar-side afferents lacking mitochondria compared to $GluA3^{WT}$ mice.

Within the afferents with mitochondria, either in $GluA3^{WT}$ or $GluA3^{KO}$ mice, the number of mitochondria varied from 1 to 9. Because the median was around 3 on average, we determined how many afferents had fewer mitochondria below the median ($n$ = 1–2 mitochondria per afferent) and how many had above the median (more than 3) (Figure 9D, right). In $GluA3^{WT}$, the percentage of modiolar-side afferent terminals with a lower and higher number of mitochondria was similar (25% and 28%, respectively). In contrast, only a small percentage (6%) of pillar-side afferent terminals had a lower number of mitochondria, whereas the majority (41%) had a higher number. In the $GluA3^{KO}$, the percentage of modiolar-side afferents with one or two mitochondria was larger than those with more than three (38% and 24%, respectively). In pillar-side afferents, 14% had one or two mitochondria, while the rest (24%) had more than three. When comparing $GluA3^{WT}$ and $GluA3^{KO}$ data, we found that in the $GluA3^{KO,}$ there was an increase in the number of modiolar and pillar side afferents with a low number of mitochondria. A larger percentage of afferent terminals without or with a lower number of mitochondria in the female $GluA3^{KO}$ could contribute to a higher IHC-ribbon synapse vulnerability to ambient sound levels.

## DISCUSSION

In the present study, we analyzed the role of the GluA3 subunit on sound encoding, AMPAR subunit composition, and pre- and post-synaptic ultrastructure of IHC-ribbon synapses in female mice in ambient or in quiet sound conditions. We found that in the female $GluA3^{KO}$ mice, merely ambient background sound levels lead to early hearing impairment (Figures 1 and 2), an increase in the number of ribbonless synapses (Figure 3), an altered intrasynaptic distribution of GluA2 and GluA4 subunits within the postsynaptic membrane (Figure 6), and afferent terminal swellings suggesting glutamate excitotoxicity (Figures 7 and S2). The excitotoxicity in afferent terminals of female $GluA3^{KO}$ potentially results from an increase in the $Ca^{2+}$ and $Na^{+}$ conductances through the AMPAR channels as a consequence of the higher GluA4:GluA2 ratio (Figures 4, 5, 6, and S1). In addition, we find that GluA3 influences the morphology of presynaptic ribbons and SVs, and of afferent terminal mitochondria content in both modiolar- and pillar-side synapses (Figures 8 and 9), all indicating that GluA3 is necessary for the development, maturation, and/or maintenance of IHC-ribbon synapses. Together, our results indicate that the AMPAR subunit GluA3 is required to prevent excitotoxicity in ambient sound levels and to maintain the normal structure of IHC synapses in young adult female mice.

### Lack of GluA3 in females increases IHC-ribbon synapse vulnerability to ambient sound

We recently found that 5-week-old $GluA3^{KO}$ males raised in ambient sound levels have normal hearing sensitivity, measured by ABR click and pure-tone thresholds and wave-1 amplitude.[6]

**Table 2. Data from single ultrathin sections of IHC-ribbon synapses from mice raised in quiet**

| | | PSD length (nm) | | Major axis (nm) | | Minor axis (nm) | | Circularity | | Roundness | | SVs size (nm) | |
|---|---|---|---|---|---|---|---|---|---|---|---|---|---|
| Genotypes | Parameters | M | P | M | P | M | P | M | P | M | P | M | P |
| $GluA3^{WT}$ | Minimum | 375 | 474 | 164 | 164 | 1 | 78 | 0.26 | 0.64 | 0.15 | 0.34 | 32 | 30 |
| | 25% Percentile | 573 | 553 | 198 | 177 | 83 | 134 | 0.62 | 0.85 | 0.34 | 0.60 | 37 | 32 |
| | Median | 679 | 680 | 226 | 217 | 99 | 146 | 0.73 | 0.91 | 0.43 | 0.72 | 38 | 34 |
| | 75% Percentile | 756 | 754 | 293 | 244 | 114 | 169 | 0.83 | 0.92 | 0.54 | 0.87 | 39 | 35 |
| | Maximum | 866 | 839 | 387 | 276 | 171 | 219 | 0.87 | 0.96 | 0.59 | 0.95 | 42 | 38 |
| | Mean | 663 | 662 | 251 | 215 | 98 | 150 | 0.71 | 0.87 | 0.42 | 0.71 | 38 | 34 |
| | Std. Deviation | 122 | 121 | 68 | 36 | 32 | 33 | 0.15 | 0.08 | 0.12 | 0.16 | 2 | 2 |
| | Coefficient of variation | 18% | 18% | 27% | 17% | 33% | 22% | 21% | 9% | 30% | 23% | 6% | 7% |
| $GluA3^{KO}$ | Minimum | 424 | 305 | 155 | 146 | 68 | 93 | 0.55 | 0.66 | 0.30 | 0.37 | 35 | 36 |
| | 25% Percentile | 635 | 446 | 198 | 182 | 92 | 105 | 0.70 | 0.81 | 0.40 | 0.52 | 38 | 38 |
| | Median | 696 | 564 | 216 | 204 | 107 | 131 | 0.78 | 0.90 | 0.46 | 0.63 | 40 | 40 |
| | 75% Percentile | 743 | 648 | 272 | 232 | 143 | 147 | 0.85 | 0.94 | 0.61 | 0.82 | 41 | 41 |
| | Maximum | 863 | 777 | 405 | 276 | 200 | 201 | 0.92 | 0.96 | 0.82 | 0.92 | 43 | 41 |
| | Mean | 678 | 552 | 236 | 207 | 118 | 132 | 0.77 | 0.87 | 0.52 | 0.66 | 39 | 40 |
| | Std. Deviation | 104 | 150 | 61 | 37 | 34 | 31 | 0.10 | 0.09 | 0.15 | 0.17 | 2 | 2 |
| | Coefficient of variation | 15% | 27% | 26% | 18% | 29% | 23% | 13% | 11% | 29% | 27% | 6% | 5% |

M, modiolar; P, pillar.

The male $GluA3^{KO}$ mice do not show hearing impairment until they reach 2 months of age.[7] Here, we show that female $GluA3^{KO}$ raised in the same ambient background sound levels have decreased wave-1 amplitude at 5 weeks of age that persists up to at least 3 months (Figure 1). This early decrease in wave-1 amplitude suggests reduced action potential synchrony in the auditory nerve, or similar synchrony in fewer activated fibers, in the female $GluA3^{KO}$ mice, most likely through a combination of pre- and post-synaptic defects. Interestingly, the increased vulnerability of the female $GluA3^{KO}$ to ambient sound was mitigated at least up to 3 months of age when mice were raised in the much quieter sound environment of 10 vs. 40 dB SPL (mean SPL for the mouse frequency range) or 40–55 vs. 55–70 dB SPL (human frequency range) (Figures 1 and 2). As far as we know, this is the first report of "noise" trauma at such relatively low SPL in rodents.

Among the potential contributors to increased hearing loss vulnerability in the absence of GluA3 is a change in AMPAR subunit composition, specifically less GluA2 or more GluA4 (Figures 3, 4, 5, and 6), likely to increase the abundance of $Ca^{+2}$-permeable AMPARs (CP-AMPARs) at the IHC-ribbon synapse. AMPARs underlie fast excitatory synaptic transmission at IHC-ribbon synapses.[29,30] The activity of AMPARs is crucial for the normal physiology of synapses and, on the other hand, for the induction of excitotoxicity.[25,31] Studies have shown that noise exposure can produce excitotoxicity through excessive release of glutamate and subsequent activation of AMPARs, specifically $Ca^{2+}$-permeable AMPARs.[21,32] AMPARs at mature IHC-ribbon synapses are assembled as tetramers composed of different combinations of GluA2–4 subunits; homotetramers can exist but are less stable energetically.[33,34] AMPARs lacking any GluA2 subunits in the tetramer are $Ca^{+2}$ permeable.[35,36] Interestingly, immunoreactivity for anti-GluA2/3 or anti-GluA2 is widely reported as present at all, or nearly all, IHC-ribbon synapses.[37–39] Although the presence of GluA2 presumably reduces overall synaptic $Na^{+}$ and $Ca^{2+}$ influx, and thus vulnerability to glutamate excitotoxicity, each synapse expresses hundreds to thousands of tetramers. This suggests that glutamate-mediated cochlear synaptopathy is exacerbated by the existence of apparently GluA2-lacking intrasynaptic nanodomains presumably containing CP-AMPARs within postsynaptic densities. Indeed, recent studies in zebrafish, rats, and mice have shown that antagonizing these CP-AMPARs can prevent AMPA-induced or noise-induced synaptopathy.[21,40]

While the full complement of AMPAR pore-forming and auxiliary subunits functioning at IHC-ribbon synapses is still undetermined, in the absence of GluA3 and GluA1,[6] the GluA2/4, GluA2/2, and GluA4/4 pairs are the only possible pore-forming dimers to dimerize into tetrameric AMPAR complexes. In our study, we find the number of paired synapses (i.e., a presynaptic ribbon paired with postsynaptic GluA2 and GluA4) was similar between $GluA3^{WT}$ and $GluA3^{KO}$ female mice in both ambient and quiet rearing by 5 weeks (Figure 3), when cochlear output was already reduced in $GluA3^{KO}$. However, the number of lone ribbons and ribbonless synapses was significantly greater in the KO, but interestingly, only if raised in ambient sound levels (Figure 3). GluA2-lacking synapses were not observed in $GluA3^{WT}$ and in less than 2% of synapses in $GluA3^{KO}$ in quiet or ambient. GluA4-lacking synapses (i.e., a presynaptic ribbon paired with postsynaptic GluA2 only) were not observed in quiet in either genotype. Ambient sound increased the occurrence of GluA4-lacking synapses in both genotypes, with significantly more in $GluA3^{WT}$ than $GluA3^{KO}$ (~30% of synapses in some images from the 10 kHz region (Figure 3). Thus, ambient sound appears to induce a shift toward GluA2-only synapses in $GluA3^{WT}$ and toward unpaired pre- and post-synaptic puncta in $GluA3^{KO}$. Both

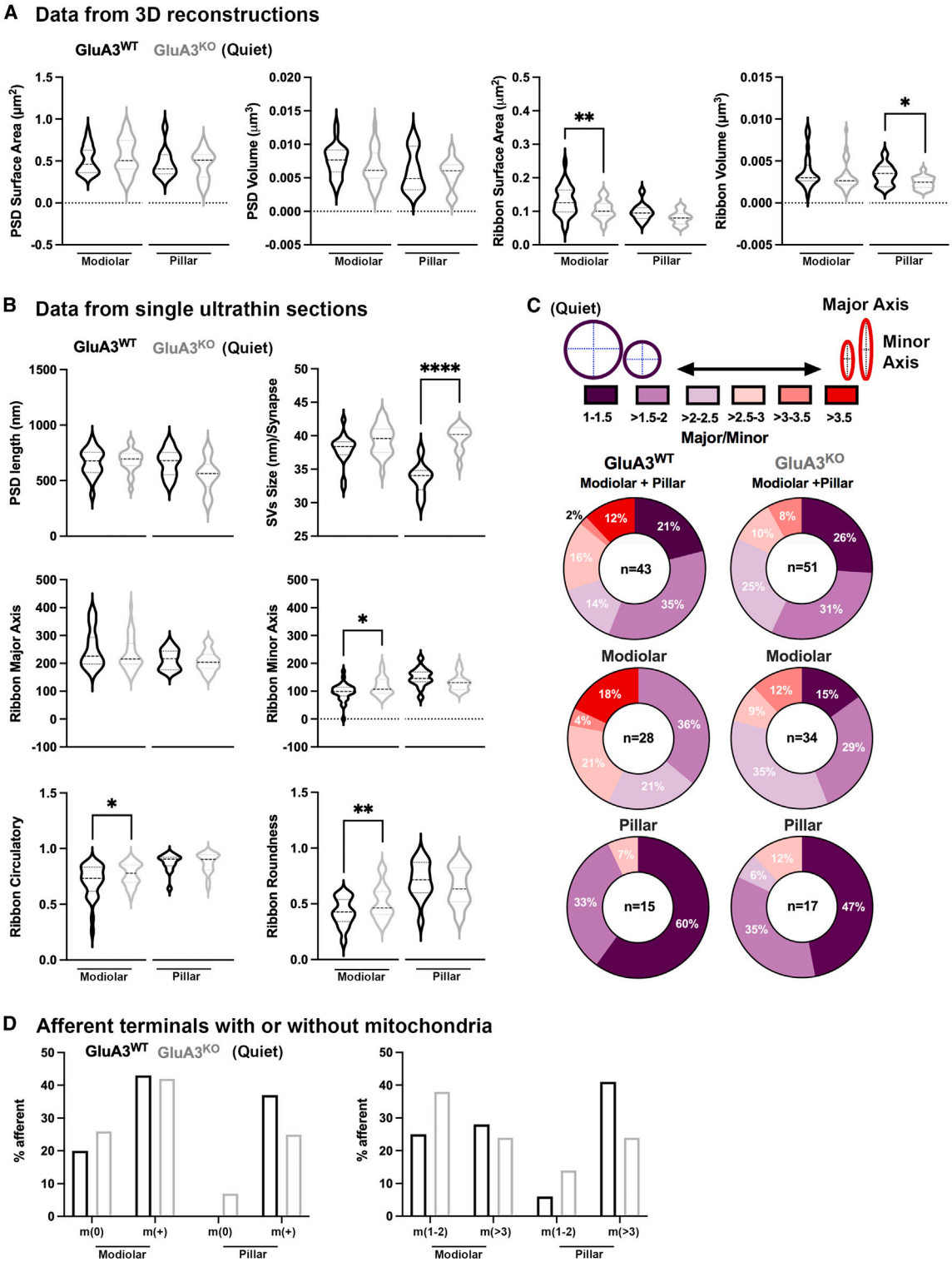


**Figure 9. Synaptic vesicle size and pre-synaptic ribbon shape are altered in the 5-week-old GluA3$^{KO}$ female mice in quiet**

(A) Violin plots show the quantitative comparison of the surface and volume of PSDs and ribbons obtained from 3D reconstruction between GluA3$^{WT}$ (black) and GluA3$^{KO}$ (gray) mice. One-way ANOVA, $*p < 0.05$. Data corresponds to median.

(B) Violin plots show the quantitative comparison of PSD length, major and minor ribbon, ribbon circularity and roundness, and synaptic vesicle (SV) size per synapse between GluA3$^{WT}$ (black) and GluA3$^{KO}$ (gray). One-way ANOVA, $*p < 0.05$, $**p < 0.01$, $***p < 0.001$, $****p < 0.0001$. Data corresponds to median.

*(legend continued on next page)*

genotypes had unpaired synapses when reared in ambient sound, but ribbonless synapses containing GluA2 and GluA4 were more abundant in GluA3$^{KO}$ (~10%) than GluA3$^{WT}$ (~5%). As well, these ribbonless synapses in GluA3$^{WT}$ tended to have greater GluA4:GluA2 ratios (implied $Ca^{2+}$ permeability) than the paired synapses in the same images, but not in GluA3$^{KO}$ or in quiet sound (Figure 4). If the presence of the ribbon in GluA3$^{WT}$ is associated with AMPARs having relatively less $Ca^{2+}$ permeability, one implication is that ambient sound recruits GluA2 to ribbon synapses in a GluA3-dependent manner, somehow making them relatively less vulnerable to excitotoxicity. In the present study, it is difficult to directly compare GluA2 or GluA4 fluorescence intensities per synapse between sound conditions because those mice were in different study cohorts (only WT and KO were directly compared); however, GluA2 fluorescence appeared to increase at paired synapses in ambient sound for both genotypes, whereas ambient sound appeared to increase GluA4 in GluA3$^{KO}$ but decrease it in GluA3$^{WT}$. In the presence of GluA3, the GluA2/3 heterodimers can be recruited to synapses without adding GluA4 subunits, but in its absence, the less energetically stable GluA2/4 is the only heterodimer. Future studies should directly compare mice raised in quiet vs. ambient sound and males vs. females in the same cohorts.

In GluA3$^{KO}$ females raised in quiet, the synapses are already elevated in GluA4:GluA2 ratio, suggesting an increase in the abundance of GluA2-lacking CP-AMPARs relative to WT (Figure 4). Intriguingly, the increase in GluA4:GluA2 ratio in GluA3$^{KO}$ females relative to WT was larger in ambient sound (~103% increase in ambient vs. ~56% increase in quiet). Remarkably, we observed afferent swellings only in female GluA3$^{KO}$ and only in ambient conditions (Figures 7 and S2), which were reminiscent of swellings reported after loud noise exposure or following cochlear perfusion with excitotoxic glutamate receptor agonists, albeit smaller in size and fewer in number.[23,25] Thus, the further increase in GluA4:GluA2 ratio as well as the increase in glutamate release between quiet and ambient seems sufficient to trigger a slowly progressing excitotoxicity in the afferent terminals. Structural features of swollen afferents include missing mitochondria, swollen endoplasmic reticulum, and decreased cytoplasm electron-density. Some swellings had a PSD in opposition to a pre-synaptic ribbon, while others lacked the ribbon. The former would likely appear as a normal paired synapse in confocal imaging, and the latter would be considered a ribbonless synapse, concurrent with the increase in ribbonless synapses observed in that condition (Figure 3). Two studies in RIBEYE knockout mice, in which IHC afferent synapses lack presynaptic ribbons[41,42] found only subtle differences in evoked exocytosis, small or insignificant differences in ABR thresholds, but significant reductions in wave-1 amplitudes. In the present study, we found a similar ABR phenotype of small or insignificant differences in thresholds but significant wave-1 reductions. Although we found significant defects in presynaptic structure, including ribbonless synapses apposed to afferent swellings, we assume that even synapses without a ribbon at the time of our observation were capable of fast and sustained exocytosis. Altogether, our results show the existence of chronic ultra-structural and physiological synaptopathy induced by ambient sound long before the synapses degenerate in the female GluA3$^{KO}$ cochlea.

## Molecular and ultrastructural changes in GluA3$^{KO}$ females are already present in quiet

Even in the absence of ambient sound, we found differences between GluA3$^{WT}$ and GluA3$^{KO}$. In addition to the greater overall GluA4:GluA2 fluorescence ratios in GluA3$^{KO}$ synapses, we find an altered intrasynaptic distribution of ratios (females in quiet, Figures 5 and 6). In GluA3$^{WT}$, the ratios tended to peak 200–400 nm from the synapse center defined by the ribbon centroid, which would be closer to the perimeter of the PSD as measured in TEM (Figure 7). This peak was less pronounced in GluA3$^{KO}$ because ratios tended to be greater near the synapse center in GluA3$^{KO}$ than in GluA3$^{WT}$. Electron tomography has localized SVs morphologically docked to the presynaptic membrane only within ~100 nm of where the synaptic ribbon is anchored to the active zone, suggesting exocytosis may be limited to within 100 nm from the ribbon surface.[43] More GluA2-lacking and presumably CP-AMPARs residing closer to the sites of glutamate release would increase their probability of opening, perhaps leading to excitotoxicity in female GluA3$^{KO}$ mice raised in ambient sound levels.

Postsynaptic $Ca^{2+}$ homeostasis is crucial to protect synapses from excitotoxic insult,[28] for which mitochondria play an important role.[26,28] Reduced buffering by mitochondria in the afferent terminals of GluA3$^{KO}$ females could contribute to afferent terminal swellings and excitotoxicity. Structural studies in cats and mice indicated that pillar-side terminals contained more and larger mitochondria than modiolar-side terminals,[44,45] potentially increasing the vulnerability of afferent terminals on the modiolar side to noise trauma. In our study, we find a similar trend in the female C57BL/6 GluA3$^{WT}$ mice raised in quiet, where pillar-side terminals contained more mitochondria than modiolar-side terminals (Figure 9D). In addition, we found that ~20% of modiolar-side but 0% of pillar-side afferent terminals in GluA3$^{WT}$ lacked mitochondria in the region of interest quantified. However, in GluA3$^{KO}$ females, on both modiolar- and pillar-side synapses we found an increase in afferent terminals either without mitochondria (within the image field of view) or with a lower number of mitochondria (Figure 9D). The afferent terminals of female GluA3$^{KO}$ raised in quiet are structurally and functionally asymptomatic (i.e., no swellings, no ABR threshold or wave-1 phenotype), but these results suggest less $Ca^{2+}$ buffering capacity, which may increase vulnerability in ambient sound.

(C) Pie charts show the variability in ribbon shape in percentage from round (red) to elongated (purple) as a total (modiolar + pillar), and then separated by modiolar and pillar-side ribbons of GluA3$^{WT}$ ($n$ = 43) and GluA3$^{KO}$ ($n$ = 51). The major axis/minor axis ratio denotes the ribbon shape regardless of the size, as explained in a schematic drawing on the top of the figure.

(D) Histograms show the percentage of modiolar and pillar side afferent terminals without and with mitochondria (m (0) and m+, respectively) in the GluA3$^{WT}$ ($n$ = 32) and GluA3$^{KO}$ ($n$ = 29) mice raised in quiet (left). The histogram on the right shows the percentage of modiolar and pillar side afferent terminals with 1–2 and more than 3 mitochondria per terminal.

Postsynaptic mitochondria are critical to the development, plasticity, and maintenance of synaptic inputs.[46] Although the link between reduced mitochondrial content and the absence of GluA3 is unclear, our results suggest that GluA3 influences modiolar- and pillar-side differences in afferent terminal mitochondrial content that emerge during development.

### Reduced modiolar-pillar spatial gradients of synaptic structural heterogeneities at IHC-ribbon synapses in GluA3$^{KO}$ mice and in female mice raised in quiet

Our recent ultrastructural and molecular-anatomical confocal imaging study of cochlear ribbon synapses in 5-week-old male GluA3$^{KO}$ mice found dysregulation of GluA2 and GluA4 subunit relative abundance and alterations in pre- and post-synaptic ultrastructure associated with an increased vulnerability to glutamatergic synaptopathy at ambient, background levels of sound.[6] These structural and molecular alterations at the cochlear ribbon synapses of pre-symptomatic 5-week-old male GluA3$^{KO}$ mice appear to be pathological, preceding the reduction in ABR wave-1 amplitudes observed at 2 months of age.[7] Among the structural alterations, we found that IHC modiolar-pillar differences (larger ribbons on the modiolar side than the pillar side) were eliminated or reversed in the male GluA3$^{KO}$. Specifically, the major axes of the modiolar-side ribbons were smaller in GluA3$^{KO}$ males. The SVs were also larger on both the modiolar and pillar sides compared to the GluA3$^{WT}$.[6] Here, our structural analysis of 5-week-old female GluA3$^{WT}$ and GluA3$^{KO}$ in ambient and quiet showed that only the female KOs raised in ambient sound levels had decreased wave-1 amplitude and the characteristic type I terminal swellings, indicating functional and structural synaptopathy (Figures 1, 2, 7, and S2). Thus, we reasoned that analyzing the structure of the IHC-ribbon synapses of the female KOs in quiet would provide a unique opportunity to identify pre-symptomatic features associated with an increased vulnerability to glutamatergic synaptopathy at ambient sound levels.

Our ultrastructural analysis of the IHC-ribbon synapses of females in quiet showed that in C57BL/6 GluA3$^{WT}$ mice, the PSD and ribbon major axis lengths of the modiolar and pillar side synapses were similar (Figures 8 and 9), differing from what we and others found in male C57BL/6 or CBA/CaJ mice[6,39] or in a (presumably male) cat raised in a low-noise chamber,[44] where modiolar side ribbons are larger, suggesting a sex dependence to this hallmark trait. In GluA3$^{KO}$ females, the modiolar-side ribbons widened due to a significant increase in the minor axis length, while pillar ribbons tended to be more elongated due to the reduced minor axis length, and no difference was observed in the ribbon major axis (Figures 8 and 9). We also found double ribbons attached to the pre-synaptic membrane of modiolar side synapses in both GluA3$^{WT}$ and GluA3$^{KO}$ (Figures 7B and 7J) as previously shown.[6,18,47] Interestingly, 3 out of 11 synapses at the pillar side had double ribbons in GluA3$^{KO}$ that suggests a delay in the maturation of ribbon synapses in the absence of GluA3. Similar to the male GluA3$^{WT}$, the SVs were larger on the modiolar side in female GluA3$^{WT}$. In GluA3$^{KO}$, the SVs on modiolar- and pillar-side synapses did not differ in size because SVs on the pillar side were larger than in WT. The length of the PSD in female GluA3$^{KO}$ mice was larger in modiolar-side synapses compared to pillar side (Figures 8 and 9). Altogether, we find that lack of GluA3 alters pre- and postsynaptic features of both modiolar- and pillar-side synapses in both sexes. However, we were surprised that the effects in the female GluA3$^{KO}$ were less prominent than in the males, especially the structural alterations of the modiolar side ribbons. This could be because the WT females appear to have less structural heterogeneity in the first place, or because we analyzed the females reared in the quiet while our previous study assessed male mice raised in ambient sound. Nonetheless, our ultrastructural analysis in females supports the role of GluA3 in maintaining pre- and post-synaptic structural features. We propose that this occurs through an unknown *trans*-synaptic mechanism during development at IHC-ribbon synapses in the cochlea and the endbulb of Held synapses in the cochlear nucleus.[6,7,48] AMPAR subunits in the cochlea may interact with the *trans*-synaptic adhesion proteins neuroligins and neurexins, which could also interact with presynaptic proteins and voltage-gated $Ca^{2+}$ channels at IHC-ribbon synapses.[49–52]

### Why are females lacking GluA3 more vulnerable to ambient sound levels than males?

Studies in mice, chinchillas, and humans reported that males are more vulnerable to noise-induced hearing loss than females.[9,11,53,54] Together with prior studies,[6,7] here we show that the opposite is true in the absence of GluA3. Taken together, our data suggest that the decreased vulnerability of female WT mice requires the presence of GluA3 at the IHC-ribbon synapse. The effect of GluA3's absence on increasing excitotoxicity in female mice reared in ambient sound may be indirect due to the decrease in GluA2 at the synapse Figures 3, 4, 5, and 6); however, this decrease in GluA2 was observed also in male GluA3$^{KO}$ mice reared in ambient sound.[6] Perhaps females have a unique requirement for GluA3, or males have a unique means of resisting excitotoxicity in its absence. GluA3 and GluA2 form the most predominant dimers in the brain,[33,34] and we assume this biophysical property extends to the inner ear, although this remains to be shown directly. We speculate that loss of GluA3 results in decreased trafficking of GluA2 to the synapse since *Gria2* RNA levels were not reduced in *Gria3$^{KO}$* mice.[6] Still, it remains unclear why the 5-week-old GluA3$^{KO}$ male mice did not exhibit a reduction in ABR wave-1 amplitudes, elevation of ABR thresholds, or terminal swellings. Recently, we showed that spiral ganglion neurons from female mice have a 2-fold higher expression of *Gria3* mRNA and larger ABR wave-1 amplitudes than male mice.[8] While *Gria2* and *Gria4* are located on autosomes, *Gria3* is on the X chromosome.[55] Therefore, it is possible that females have more GluA3 due to incomplete X-inactivation in some or all SGNs, leading to increased gene dosage.[56,57] If so, knocking out *Gria3* could have a greater impact on the female than the male IHC-ribbon synapse.

### Limitations of the study

The present study confirmed that the presence of GluA3 subunits at IHC-ribbon synapses is required for the development, maturation, and maintenance of normal hearing function, the structure of the synapse, and the intrasynaptic AMPA receptor distribution. As well, it revealed a sex-dependent phenotype.

Future studies should ask what determines the sex-specific effects and directly probe synapse function at the cellular level.

## RESOURCE AVAILABILITY

### Lead contact

Further information and requests for resources and reagents should be directed to and will be fulfilled by the lead contact, María Eulalia Rubio (mer@pitt.edu).

### Materials availability

This study did not generate new unique reagents.

### Data and code availability

- All data reported in this paper will be shared by the lead contact upon request as of the date of publication.
- This paper does not include original code.
- Any additional information required to reanalyze the data reported in this paper is available from the contact upon request.

## ACKNOWLEDGMENTS

This work was supported by NIDCD DC013048 (M.E.R.) and NIDCD DC14712 (M.A.R.).

## AUTHOR CONTRIBUTIONS

M.E.R and M.A.R. designed research, performed research, analyzed data, and wrote and edited the manuscript. I.P. performed research, analyzed data, wrote the first draft, and edited the manuscript. A.B. analyzed data and edited the manuscript. M.X. performed research and edited the manuscript. E.D.W. analyzed data and edited the manuscript. B.V-G. designed and developed custom analytical tools.

## DECLARATION OF INTERESTS

The authors declare no competing interests.

## STAR★METHODS

Detailed methods are provided in the online version of this paper and include the following:

- KEY RESOURCES TABLE
- EXPERIMENTAL MODEL AND SUBJECT PARTICIPANT DETAILS
  - Animals
- METHOD DETAILS
  - Auditory brainstem recordings (*ABRs)*
  - Immunofluorescence
  - Confocal microscopy and image analysis
  - Airyscan confocal microscopy and image analysis
  - Transmission electron microscopy (TEM)
  - Morphometric analysis of TEM micrographs
- QUANTIFICATION AND STATISTICAL ANALYSIS

## SUPPLEMENTAL INFORMATION

Supplemental information can be found online at https://doi.org/10.1016/j.isci.2025.111799.

Received: June 25, 2024
Revised: November 12, 2024
Accepted: January 9, 2025
Published: January 13, 2025

## REFERENCES

1. Shanks, N.F., Savas, J.N., Maruo, T., Cais, O., Hirao, A., Oe, S., Ghosh, A., Noda, Y., Greger, I.H., Yates, J.R., and Nakagawa, T. (2012). Differences in AMPA and kainate receptor interactomes facilitate identification of AMPA receptor auxiliary subunit GSG1L. Cell Rep. *1*, 590–598. https://doi.org/10.1016/j.celrep.2012.05.004.
2. Bassani, S., Folci, A., Zapata, J., and Passafaro, M. (2013). AMPAR trafficking in synapse maturation and plasticity. Cell. Mol. Life Sci. *70*, 4411–4430. https://doi.org/10.1007/s00018-013-1309-1.
3. Purkey, A.M., and Dell'Acqua, M.L. (2020). Phosphorylation-Dependent Regulation of Ca2+-Permeable AMPA Receptors During Hippocampal Synaptic Plasticity. Front. Synaptic Neurosci. *12*, 8. https://doi.org/10.3389/fnsyn.2020.00008.
4. Wang, Y.X., Wenthold, R.J., Ottersen, O.P., and Petralia, R.S. (1998). Endbulb synapses in the anteroventral cochlear nucleus express a specific subset of AMPA-type glutamate receptor subunits. J. Neurosci. *18*, 1148–1160. https://doi.org/10.1523/JNEUROSCI.18-03-01148.1998.
5. Rubio, M.E., Matsui, K., Fukazawa, Y., Kamasawa, N., Harada, H., Itakura, M., Molnár, E., Abe, M., Sakimura, K., and Shigemoto, R. (2017). The number and distribution of AMPA receptor channels containing fast kinetic GluA3 and GluA4 subunits at auditory nerve synapses depend on the target cells. Brain Struct. Funct. *222*, 3375–3393. https://doi.org/10.1007/s00429-017-1408-0.
6. Rutherford, M.A., Bhattacharyya, A., Xiao, M., Cai, H.-M., Pal, I., and Rubio, M.E. (2023). GluA3 subunits are required for appropriate assembly of AMPAR GluA2 and GluA4 subunits on cochlear afferent synapses and for presynaptic ribbon modiolar-pillar morphology. Elife *12*, e80950. https://doi.org/10.7554/eLife.80950.
7. García-Hernández, S., Abe, M., Sakimura, K., and Rubio, M.E. (2017). Impaired auditory processing and altered structure of the endbulb of Held synapse in mice lacking the GluA3 subunit of AMPA receptors. Hear. Res. *344*, 284–294. https://doi.org/10.1016/j.heares.2016.12.006.
8. Lozier, N.R., Muscio, S., Pal, I., Cai, H.-M., and Rubio, M.E. (2023). Sex differences in glutamate AMPA receptor subunits mRNA with fast gating kinetics in the mouse cochlea. Front. Syst. Neurosci. *17*, 1100505. https://doi.org/10.3389/fnsys.2023.1100505.
9. Milon, B., Mitra, S., Song, Y., Margulies, Z., Casserly, R., Drake, V., Mong, J.A., Depireux, D.A., and Hertzano, R. (2018). The impact of biological sex on the response to noise and otoprotective therapies against acoustic injury in mice. Biol. Sex Differ. *9*, 12. https://doi.org/10.1186/s13293-018-0171-0.
10. Rouse, S.L., Matthews, I.R., Li, J., Sherr, E.H., and Chan, D.K. (2020). Integrated stress response inhibition provides sex-dependent protection against noise-induced cochlear synaptopathy. Sci. Rep. *10*, 18063. https://doi.org/10.1038/s41598-020-75058-w.
11. Shuster, B., Casserly, R., Lipford, E., Olszewski, R., Milon, B., Viechweg, S., Davidson, K., Enoch, J., McMurray, M., Rutherford, M.A., et al. (2021). Estradiol Protects against Noise-Induced Hearing Loss and Modulates Auditory Physiology in Female Mice. Int. J. Mol. Sci. *22*, 12208. https://doi.org/10.3390/ijms222212208.
12. Li, N., and Carrel, L. (2008). Escape from X chromosome inactivation is an intrinsic property of the Jarid1c locus. Proc. Natl. Acad. Sci. USA *105*, 17055–17060. https://doi.org/10.1073/pnas.0807765105.
13. Abdala, C., and Dhar, S. (2012). Maturation and Aging of the Human Cochlea: A View through the DPOAE Looking Glass. J. Assoc. Res. Otolaryngol. *13*, 403–421. https://doi.org/10.1007/s10162-012-0319-2.
14. Konrad-Martin, D., Dille, M.F., McMillan, G., Griest, S., McDermott, D., Fausti, S.A., and Austin, D.F. (2012). Age-related changes in the auditory brainstem response. J. Am. Acad. Audiol. *23*, 18–75. https://doi.org/10.3766/jaaa.23.1.3.
15. Johannesen, P.T., and Lopez-Poveda, E.A. (2021). Age-related central gain compensation for reduced auditory nerve output for people with

normal audiograms, with and without tinnitus. iScience *24*, 102658. https://doi.org/10.1016/j.isci.2021.102658.

16. Rutherford, M.A., and Moser, T. (2016). The Ribbon Synapse Between Type I Spiral Ganglion Neurons and Inner Hair Cells. In The Primary Auditory Neurons of the Mammalian Cochlea, A. Dabdoub, B. Fritzsch, A.N. Popper, and R.R. Fay, eds. (Springer), pp. 117–156. https://doi.org/10.1007/978-1-4939-3031-9_5.
17. Kim, K.X., and Rutherford, M.A. (2016). Maturation of NaV and KV Channel Topographies in the Auditory Nerve Spike Initiator before and after Developmental Onset of Hearing Function. J. Neurosci. *36*, 2111–2118. https://doi.org/10.1523/JNEUROSCI.3437-15.2016.
18. Payne, S.A., Joens, M.S., Chung, H., Skigen, N., Frank, A., Gattani, S., Vaughn, K., Schwed, A., Nester, M., Bhattacharyya, A., et al. (2021). Maturation of Heterogeneity in Afferent Synapse Ultrastructure in the Mouse Cochlea. Front. Synaptic Neurosci. *13*, 678575. https://doi.org/10.3389/fnsyn.2021.678575.
19. Wong, A.B., Jing, Z., Rutherford, M.A., Frank, T., Strenzke, N., and Moser, T. (2013). Concurrent maturation of inner hair cell synaptic Ca2+ influx and auditory nerve spontaneous activity around hearing onset in mice. J. Neurosci. *33*, 10661–10666. https://doi.org/10.1523/JNEUROSCI.1215-13.2013.
20. Wong, A.B., Rutherford, M.A., Gabrielaitis, M., Pangršič, T., Göttfert, F., Frank, T., Michanski, S., Hell, S., Wolf, F., Wichmann, C., and Moser, T. (2014). Developmental refinement of hair cell synapses tightens the coupling of Ca2+ influx to exocytosis. EMBO J. *33*, 247–264. https://doi.org/10.1002/embj.201387110.
21. Hu, N., Rutherford, M.A., and Green, S.H. (2020). Protection of cochlear synapses from noise-induced excitotoxic trauma by blockade of Ca2+--permeable AMPA receptors. Proc. Natl. Acad. Sci. USA *117*, 3828–3838. https://doi.org/10.1073/pnas.1914247117.
22. Ohlemiller, K.K., and Gagnon, P.M. (2004). Apical-to-basal gradients in age-related cochlear degeneration and their relationship to "primary" loss of cochlear neurons. J. Comp. Neurol. *479*, 103–116. https://doi.org/10.1002/cne.20326.
23. Robertson, D. (1983). Functional significance of dendritic swelling after loud sounds in the guinea pig cochlea. Hear. Res. *9*, 263–278. https://doi.org/10.1016/0378-5955(83)90031-x.
24. Puel, J.L., Pujol, R., Tribillac, F., Ladrech, S., and Eybalin, M. (1994). Excitatory amino acid antagonists protect cochlear auditory neurons from excitotoxicity. J. Comp. Neurol. *341*, 241–256. https://doi.org/10.1002/cne.903410209.
25. Puel, J.L., Ruel, J., Gervais d'Aldin, C., and Pujol, R. (1998). Excitotoxicity and repair of cochlear synapses after noise-trauma induced hearing loss. Neuroreport *9*, 2109–2114. https://doi.org/10.1097/00001756-199806220-00037.
26. Duchen, M.R. (2000). Mitochondria and calcium: from cell signalling to cell death. J. Physiol. *529*, 57–68. https://doi.org/10.1111/j.1469-7793.2000.00057.x.
27. Matuz-Mares, D., González-Andrade, M., Araiza-Villanueva, M.G., Vilchis-Landeros, M.M., and Vázquez-Meza, H. (2022). Mitochondrial Calcium: Effects of Its Imbalance in Disease. Antioxidants *11*, 801. https://doi.org/10.3390/antiox11050801.
28. Verma, M., Lizama, B.N., and Chu, C.T. (2022). Excitotoxicity, calcium and mitochondria: a triad in synaptic neurodegeneration. Transl. Neurodegener. *11*, 3. https://doi.org/10.1186/s40035-021-00278-7.
29. Ruel, J., Chen, C., Pujol, R., Bobbin, R.P., and Puel, J.L. (1999). AMPA-preferring glutamate receptors in cochlear physiology of adult guinea-pig. J. Physiol. *518*, 667–680. https://doi.org/10.1111/j.1469-7793.1999.0667p.x.
30. Glowatzki, E., and Fuchs, P.A. (2002). Transmitter release at the hair cell ribbon synapse. Nat. Neurosci. *5*, 147–154. https://doi.org/10.1038/nn796.
31. Ruel, J., Bobbin, R.P., Vidal, D., Pujol, R., and Puel, J.L. (2000). The selective AMPA receptor antagonist GYKI 53784 blocks action potential generation and excitotoxicity in the guinea pig cochlea. Neuropharmacology *39*, 1959–1973. https://doi.org/10.1016/s0028-3908(00)00069-1.
32. Kim, K.X., Payne, S., Yang-Hood, A., Li, S.-Z., Davis, B., Carlquist, J., V-Ghaffari, B., Gantz, J.A., Kallogjeri, D., Fitzpatrick, J.A.J., et al. (2019). Vesicular Glutamatergic Transmission in Noise-Induced Loss and Repair of Cochlear Ribbon Synapses. J. Neurosci. *39*, 4434–4447. https://doi.org/10.1523/JNEUROSCI.2228-18.2019.
33. Rossmann, M., Sukumaran, M., Penn, A.C., Veprintsev, D.B., Babu, M.M., and Greger, I.H. (2011). Subunit-selective N-terminal domain associations organize the formation of AMPA receptor heteromers. EMBO J. *30*, 959–971. https://doi.org/10.1038/emboj.2011.16.
34. Zhao, H., Lomash, S., Chittori, S., Glasser, C., Mayer, M.L., and Schuck, P. (2017). Preferential assembly of heteromeric kainate and AMPA receptor amino terminal domains. Elife *6*, e32056. https://doi.org/10.7554/eLife.32056.
35. Hollmann, M., Hartley, M., and Heinemann, S. (1991). Ca2+ permeability of KA-AMPA–gated glutamate receptor channels depends on subunit composition. Science *252*, 851–853. https://doi.org/10.1126/science.1709304.
36. Geiger, J.R., Melcher, T., Koh, D.S., Sakmann, B., Seeburg, P.H., Jonas, P., and Monyer, H. (1995). Relative abundance of subunit mRNAs determines gating and Ca2+ permeability of AMPA receptors in principle neurons and interneurons in rat CNS. Neuron *15*, 193–204. https://doi.org/10.1016/0896-6273(95)90076-4.
37. Khimich, D., Nouvian, R., Pujol, R., Tom Dieck, S., Egner, A., Gundelfinger, E.D., and Moser, T. (2005). Hair cell synaptic ribbons are essential for synchronous auditory signalling. Nature *434*, 889–894. https://doi.org/10.1038/nature03418.
38. Meyer, A.C., Frank, T., Khimich, D., Hoch, G., Riedel, D., Chapochnikov, N.M., Yarin, Y.M., Harke, B., Hell, S.W., Egner, A., and Moser, T. (2009). Tuning of synapse number, structure and function in the cochlea. Nat. Neurosci. *12*, 444–453. https://doi.org/10.1038/nn.2293.
39. Liberman, L.D., Wang, H., and Liberman, M.C. (2011). Opposing gradients of ribbon size and AMPA receptor expression underlie sensitivity differences among cochlear-nerve/hair-cell synapses. J. Neurosci. *31*, 801–808. https://doi.org/10.1523/JNEUROSCI.3389-10.2011.
40. Sebe, J.Y., Cho, S., Sheets, L., Rutherford, M.A., von Gersdorff, H., and Raible, D.W. (2017). Ca2+-Permeable AMPARs Mediate Glutamatergic Transmission and Excitotoxic Damage at the Hair Cell Ribbon Synapse. J. Neurosci. *37*, 6162–6175. https://doi.org/10.1523/JNEUROSCI.3644-16.2017.
41. Becker, L., Schnee, M.E., Niwa, M., Sun, W., Maxeiner, S., Talaei, S., Kachar, B., Rutherford, M.A., and Ricci, A.J. (2018). The presynaptic ribbon maintains vesicle populations at the hair cell afferent fiber synapse. Elife *7*, e30241. https://doi.org/10.7554/eLife.30241.
42. Jean, P., Lopez de la Morena, D., Michanski, S., Jaime Tobón, L.M., Chakrabarti, R., Picher, M.M., Neef, J., Jung, S., Gültas, M., Maxeiner, S., et al. (2018). The synaptic ribbon is critical for sound encoding at high rates and with temporal precision. Elife *7*, e29275. https://doi.org/10.7554/eLife.29275.
43. Chakrabarti, R., Fung, T.S., Kang, T., Elonkirjo, P.W., Suomalainen, A., Usherwood, E.J., and Higgs, H.N. (2022). Mitochondrial dysfunction triggers actin polymerization necessary for rapid glycolytic activation. J. Cell Biol. *221*, e202201160. https://doi.org/10.1083/jcb.202201160.
44. Liberman, M.C. (1980). Morphological differences among radial afferent fibers in the cat cochlea: an electron-microscopic study of serial sections. Hear. Res. *3*, 45–63. https://doi.org/10.1016/0378-5955(80)90007-6.
45. Moverman, D.J., Liberman, L.D., Kraemer, S., Corfas, G., and Liberman, M.C. (2023). Ultrastructure of noise-induced cochlear synaptopathy. Sci. Rep. *13*, 19456. https://doi.org/10.1038/s41598-023-46859-6.

46. Thomas, C.I., Ryan, M.A., Kamasawa, N., and Scholl, B. (2023). Postsynaptic mitochondria are positioned to support functional diversity of dendritic spines. Elife *12*, RP89682. https://doi.org/10.7554/eLife.89682.

47. Michanski, S., Smaluch, K., Steyer, A.M., Chakrabarti, R., Setz, C., Oestreicher, D., Fischer, C., Möbius, W., Moser, T., Vogl, C., and Wichmann, C. (2019). Mapping developmental maturation of inner hair cell ribbon synapses in the apical mouse cochlea. Proc. Natl. Acad. Sci. USA *116*, 6415–6424. https://doi.org/10.1073/pnas.1812029116.

48. Antunes, F.M., Rubio, M.E., and Kandler, K. (2020). Role of GluA3 AMPA Receptor Subunits in the Presynaptic and Postsynaptic Maturation of Synaptic Transmission and Plasticity of Endbulb-Bushy Cell Synapses in the Cochlear Nucleus. J. Neurosci. *40*, 2471–2484. https://doi.org/10.1523/JNEUROSCI.2573-19.2020.

49. Araç, D., Boucard, A.A., Ozkan, E., Strop, P., Newell, E., Südhof, T.C., and Brunger, A.T. (2007). Structures of neuroligin-1 and the neuroligin-1/neurexin-1 beta complex reveal specific protein-protein and protein-Ca2+ interactions. Neuron *56*, 992–1003. https://doi.org/10.1016/j.neuron.2007.12.002.

50. Luo, F., Sclip, A., Jiang, M., and Südhof, T.C. (2020). Neurexins cluster Ca2+ channels within the presynaptic active zone. EMBO J. *39*, e103208. https://doi.org/10.15252/embj.2019103208.

51. Ramirez, M.A., Ninoyu, Y., Miller, C., Andrade, L.R., Edassery, S., Bomba-Warczak, E., Ortega, B., Manor, U., Rutherford, M.A., Friedman, R.A., and Savas, J.N. (2022). Cochlear ribbon synapse maturation requires Nlgn1 and Nlgn3. iScience *25*, 104803. https://doi.org/10.1016/j.isci.2022.104803.

52. Jukic, A., Lei, Z., Cebul, E.R., Pinter, K., Mosqueda, N., David, S., Tarchini, B., and Kindt, K. (2024). Presynaptic Nrxn3 is essential for ribbon-synapse assembly in hair cells. Preprint at bioRxiv. https://doi.org/10.1101/2024.02.14.580267.

53. McFadden, S.L., Zheng, X.Y., and Ding, D.L. (2000). Conditioning-induced protection from impulse noise in female and male chinchillas. J. Acoust. Soc. Am. *107*, 2162–2168. https://doi.org/10.1121/1.428497.

54. Szanto, C., and Ionescu, M. (1983). Influence of age and sex on hearing threshold levels in workers exposed to different intensity levels of occupational noise. Audiology *22*, 339–356. https://doi.org/10.3109/00206098309072794.

55. Mahadevaiah, S.K., Royo, H., VandeBerg, J.L., McCarrey, J.R., Mackay, S., and Turner, J.M.A. (2009). Key features of the X inactivation process are conserved between marsupials and eutherians. Curr. Biol. *19*, 1478–1484. https://doi.org/10.1016/j.cub.2009.07.041.

56. Carrel, L., and Willard, H.F. (2005). X-inactivation profile reveals extensive variability in X-linked gene expression in females. Nature *434*, 400–404. https://doi.org/10.1038/nature03479.

57. Berletch, J.B., Ma, W., Yang, F., Shendure, J., Noble, W.S., Disteche, C.M., and Deng, X. (2015). Identification of genes escaping X inactivation by allelic expression analysis in a novel hybrid mouse model. Data Brief *5*, 761–769. https://doi.org/10.1016/j.dib.2015.10.033.

58. Jing, Z., Rutherford, M.A., Takago, H., Frank, T., Fejtova, A., Khimich, D., Moser, T., and Strenzke, N.J. (2013). Disruption of the presynaptic cytomatrix protein bassoon degrades ribbon anchorage, multiquantal release, and sound encoding at the hair cell afferent synapse. J. Neurosci. *33*, 4456–4467. https://doi.org/10.1523/JNEUROSCI.3491-12.2013.

59. Ohn, T.-L., Rutherford, M.A., Jing, Z., Jung, S., Duque-Alonso, C.J., Hoch, G., Picher, M.M., Scharinger, A., Strenzke, N.M., and Moser, T. (2016). Hair cells use active zones with different voltage dependence of Ca2+ influx to decompose sounds into complementary neural codes. Proc. Natl. Acad. Sci. USA *113*, E4716–E4725. https://doi.org/10.1073/pnas.1605737113.

60. Müller, M., von Hünerbein, K., Hoidis, S., and Smolders, J.W. (2005). A physiological place-frequency map of the cochlea in the CBA/J mouse. Hear. Res. https://doi.org/10.1016/j.heares.2004.08.011.

61. Rutherford, M.A. (2015). Resolving the structure of inner ear ribbon synapses with STED microscopy. Synapse *69*, 242–255. https://doi.org/10.1002/syn.21812.

62. Gómez-Nieto, R., and Rubio, M.E. (2009). A bushy cell network in the rat ventral cochlear nucleus. J. Comp. Neurol. *516*, 241–263. https://doi.org/10.1002/cne.22139.

## STAR★METHODS

### KEY RESOURCES TABLE

| REAGENT or RESOURCE | SOURCE | IDENTIFIER |
|---|---|---|
| Antibodies | | |
| CtBP2 | BD Transduction Laboratories | Cat# 612,044; RRID: AB_399431 |
| GluA2 | Millipore | Cat# MAB397; RRID: AB_2113875 |
| GluA3 | Santa Cruz Biotechnology | Cat# Sc-7612; RRID: AB_2113895 |
| GluA4 | Millipore | Cat# AB1508; RRID: AB_90711 |
| Alexa Fluor 488 | Thermo Fisher Scientific | Cat# A-21206; RRID: AB_2535792 |
| Alexa Fluor 555 | Thermo Fisher Scientific | Cat# A-21127; RRID: AB_2535769 |
| Alexa Fluor 647 | Thermo Fisher Scientific | Cat# A-21241; RRID: AB_2535810 |
| Chemicals, peptides, and recombinant proteins | | |
| Paraformaldehyde | Electron microscopy Sciences | Cat# 19210 |
| Ketamine hydrochloride | Covetrus | Cat# 071069 |
| Xylazine | Rompun | Cat# 047-956 |
| Triton X-100 | Sigma | Cat# T9284 |
| EDTA | BIO-RAD | Cat# 1610729 |
| Horse serum | Vector Laboratories | Cat# S-2000 |
| DAPI | Invitrogen | Cat# P36931 |
| Sodium phosphate monobasic | Signa-Aldrich | Cat# S9638 |
| Sodium phosphate dibasic | Signa-Aldrich | Cat# S9763 |
| Sodium chloride | Fisher bioreagents | Cat# BP358-1 |
| Isoflurane | Piramal Critical Care Inc | Cat# 66794-0017-25 |
| Glutaraldehyde | Electron microscopy Sciences | Cat# 16320 |
| Ethanol | Electron microscopy Sciences | Cat# 15055 |
| Acetonitrile | Electron microscopy Sciences | Cat# 10020 |
| Sodium Cacodylate salt | Electron microscopy Sciences | Cat# 12300 |
| Osmium tetraoxide 4% | Electron microscopy Sciences | Cat# 19150 |
| Potassium ferrocyanide | Electron microscopy Sciences | Cat# 20150 |
| Uranyl acetate | Electron microscopy Sciences | Cat# 22400 |
| Formvar Solution | Electron microscopy Sciences | Cat# 15820 |
| Critical commercial assays | | |
| EMBed-812 Embedding Kit | Electron microscopy Sciences | Cat# 14120 |
| Experimental models: Organisms/strains | | |
| Mouse: Gria3$^{KO}$: C57BL/6J | García-Hernández et al. 2017[7] | N/A |
| Mouse: Gria3$^{WT}$: C57BL/6J | Jackson lab | N/A |
| Software and algorithms | | |
| BioSigRP | Tucker Davis Technologies | Version 5.7.3 |
| Reconstruct | SynapseWeb | Version 1.1.0.0 https://synapseweb.clm.utexas.edu/software-0 |
| ImageJ | NIH | https://fiji.sc/ |
| Prism 9.4.1 | Graphpad | https://www.graphpad.com/features |
| Imaris | Bitplane | https://imaris.oxinst.com |
| ZEN 2012 | Zeiss | https://www.zeiss.com/microscopy/us/products/software/zeiss-zen.html |
| Adobe Photoshop | Adobe | https://www.adobe.com/products/photoshop.html |

(*Continued on next page*)

*Continued*

| REAGENT or RESOURCE | SOURCE | IDENTIFIER |
|---|---|---|
| IGOR Pro 7.08 | WaveMetrics | https://www.wavemetrics.com/software/igor-pro-708-installer |
| Other | | |
| ABR System | Tucker-Davis Technologies | https://www.tdt.com |
| Thermometer | Kent Scientific Corporation | https://www.kentscientific.com/products/type-jkt-thermocouple-meter/?srsltid=AfmBOoorHXpzkTFzC9DkH-BWe-AZ43kxeUZG1F1kOiT7r3aY26s02w0P |
| Multi-field magnetic speaker | Tucker-Davis Technologies | https://www.tdt.com |
| Isoflurane Vaporizer | G.A.S. | https://generalanestheticservices.com |
| Ultramicrotome | Leica | N/A |
| Transmission Electron Microscope | JEOL Ltd. | N/A |
| Airyscan Confocal | Zeiss | N/A |

## EXPERIMENTAL MODEL AND SUBJECT PARTICIPANT DETAILS

### Animals

In this study, a total of 57 female C57BL/6 wild type (GluA3$^{WT}$, $n = 26$) and GluA3-knockout (GluA3$^{KO}$, $n = 31$) mice from two different colonies were used between postnatal days 20 (P20, 3-week) to 90 (P90, 13-week). The generation of the GluA3$^{KO}$ mice has been previously described.[5,7] Mice were raised up to P20 in quiet sound pressure level conditions (40–55 dB SPL, 100 Hz–8.3 kHz, general audible range for humans, measured with an audiometer, General Tools & Instruments LLC; 10 dB SPL, 3 kHz–90 kHz, mouse hearing range, Sensory Sentinel, Turner Scientific, Jacksonville, IL). One group of GluA3$^{WT}$ ($n = 13$) and *GluA3*$^{KO}$ ($n = 14$) mice were maintained in the same quiet conditions until P90 (Figure 1A). A second group of mice (GluA3$^{WT}$ $n = 13$) and (GluA3$^{KO}$ $n = 17$) were moved at P20 to a room facility with ambient sound pressure levels (55–75 dB SPL, 100 Hz–8.3 kHz, general audible range for humans measured with an audiometer; 40 dB SPL, 3 kHz–90 kHz, mouse hearing range, Sensory Sentinel) and maintained until they reached P90 (Figure 1A). Both mouse groups were reared in a 12-h light/12-h dark daily photoperiod and were fed *ad libitum*. Auditory brainstem recordings (ABRs) were collected at four postnatal days: P20, P35, P60, and P90. Cochleae were dissected from P35 mice and used for further experiments (Figure 1A). All experimental procedures were per the National Institute of Health guidelines and approved by the University of Pittsburgh Institutional Animal Care and Use Committee.

## METHOD DETAILS

### Auditory brainstem recordings (*ABRs*)

At least 10–15 GluA3$^{WT}$ and GluA3$^{KO}$ mice from each animal group (quiet and ambient) and age group were used for ABRs. During the ABRs, mice were kept anesthetized with isoflurane (3% induction and 1.5% maintenance), and the internal temperature was monitored with a thermometer (J/K/T Thermocouple, Kent Scientific Corporation) that was kept constant between 37 and 38°C using isothermal heat pads. Open-field ABRs and analysis were performed as described.[8] Briefly, ABRs were recorded in a sound attenuation chamber inside a Faraday cage. The speaker was calibrated in the chamber using a microphone (PCB electronics, model no. 377C01, Depew, NY) placed 10 cm from the multi-field magnetic speaker (MF1, Tucker-Davis Technologies (TDT), Alachua, FL), which was the same distance as the mouse's external ear to the speaker during experiments. For ABR recordings, needle electrodes were placed subcutaneously at the vertex of the scalp and below the pinna of both the tested (ipsilateral) and contralateral ears. Clicks (1 ms) or pure tones of 4, 8, 12, 16, 24, and 32 kHz (0.5 ms) stimuli were presented from 90 dB to 10 dB in decreasing steps of 5 dB at 21 sweeps with an interstimulus interval of 47.6 ms. All the recordings' responses were averaged over 512 sweeps, amplified, digitized, and transferred via an optical port to the RZ6 processor. ABR click, and pure tone thresholds were determined as the lowest intensity level (in dB SPL) at which reproducible peaks were visible. The clicks wave I amplitude (in μV) was determined as the difference between the peak and subsequent trough.

### Immunofluorescence

A total of 9 female mice (GluA3$^{WT}$ $n = 4$; GluA3$^{KO}$ $n = 5$) at 5 weeks of age, raised in either ambient sound (ambient group) or low-level sound (quiet group) were anesthetized with ketamine (60 mg/kg) and xylazine (6.5 mg/kg), then perfused intravascularly for 10 min with fixative consisting of 4% paraformaldehyde (PFA) in 0.1M phosphate buffer (PB), pH = 7.2. Temporal bones were then isolated from the skull, the stapes was removed, the oval and round window membranes were punctured, and a hole was opened at the apex of the cochlear bone near the helicotrema. Each cochlea was perfused with fixative through the oval window while bathing in a dish of

fixative. After postfixation for 45 min in the dish on top of an ice pack, the cochleae were rinsed in 0.1M phosphate-buffered saline (PBS) and then shipped to Washington University in St. Louis overnight in PB supplemented with 5% glycerol.

GluA3$^{WT}$ and GluA3$^{KO}$ cochleae were batch processed in parallel using the same reagent solutions in two separate groups, one raised in ambient background sound and the other raised in quiet background sound levels. After rinsing in PB, each temporal bone was decalcified in 50 mL of PB supplemented with 10% EDTA for 2 h at room temperature on a rocker. After removing the outer shell of the cochlea and peeling away the lateral wall, the spiral containing the organ of Corti, osseous spiral lamina, and spiral ganglion was isolated and cut into apical-cochlear, middle-cochlear, and basal-cochlear pieces for wholemount immunolabeling as previously described.[6,17,21,32,40,58,59] To permeabilize the tissue and to block non-specific binding of antibodies, the samples were immersed overnight at 4°C in 100 μL of blocking buffer (0.3% Triton X-100 and 16% normal horse serum in PBS) in a 9-well Pyrex glass plate. To label presynaptic ribbons (CtBP2/Ribeye) and postsynaptic AMPA-type glutamate receptor subunits (GluA2, GluA3, and GluA4), primary antibodies were diluted in blocking buffer (1:400) and samples were incubated in the 9-well plates with 100 μL per plate overnight at 4°C: CtBP2 mouse IgG1 (BD Biosciences 612044; RRID:AB_399431), GluA2 mouse IgG2a (Millipore MAB397; RRID:AB_2113875), GluA3 goat (Santa Cruz Biotechnology SC7612), and GluA4 rabbit (Millipore AB1508; RRID:AB_90711). After rinsing 3 times in wash buffer (PBS supplemented with 0.3% Triton X-), samples were incubated for 1 h at room temperature in species-appropriate secondary antibodies diluted in blocking buffer (1:100). Secondary antibodies were pre-conjugated to Alexa Fluor (Life Tech.) fluorophores excited by 488, 555, or 647 nm light. After rinsing 3 times in wash buffer and PBS, the 3 pieces from each cochlea were mounted in Mowöl between a microscope slide and coverslips (#1.5, Zeiss). Slides were kept at 4°C until imaging.

## Confocal microscopy and image analysis

Confocal volumes were acquired with 12-bit images, 100 μm wide containing approximately 12 IHCs, on a Zeiss LSM 700 with a 63X 1.4 NA oil objective lens with a Z-step of 0.37 μm and pixel size of 50 nm in X and Y, and a pinhole setting of 1 AU. We first surveyed the samples to determine the necessary laser power settings to collect all the images at a gain of 700 while avoiding pixel intensity saturation. Using identical acquisition settings across samples, we collected 3–4 images from the center of each of the 3 pieces (basal-, middle-, and apical-cochlear) near tonotopic characteristic frequencies of 10, 20, and 40 kHz.[60] For display only, the brightness and contrast levels were adjusted linearly for visual clarity. Image analysis was performed on raw data.

The numbers of hair cells and synapses were counted and manually verified after semi-automated identification using Imaris software (Bitplane) to calculate the mean number of synapses per IHC per image. The observers were blinded to mouse genotype. For each group of images, group means (±SD) were calculated across image means. Paired synapses were identified as juxtaposed puncta of presynaptic ribbons (Ribeye/CtBP2) and postsynaptic AMPA receptor patches (GluA2 and/or GluA4), which appear to partly overlap at confocal resolution.[61] Unpaired (i.e., lone) ribbons were defined as Ribyey/CtBP2 puncta located under inner hair cell nuclei, in the synaptic region, but lacking apposed GluA2 or GluA4 puncta. Inner hair cell nuclei were labeled with CtBP2/Ribeye because CtBP2 is a transcriptional co-repressor. For unpaired ribbons, we did not distinguish membrane-anchored from unanchored. Ribbonless synapses consisted of GluA2 and/or GluA4 puncta located in the synaptic region under the inner hair cell nuclei but lacking apposed presynaptic ribbons.

Pixels comprising puncta of synaptic fluorescence were segmented in 3D as 'surface' objects in Imaris using identical settings across image stacks, including the 'local contrast background subtraction' setting to automatically calculate the appropriate pixel-intensity threshold for each fluorescence channel in each image. This adaptive and automatically calculated thresholding algorithm compensated for differences in overall luminance between image stacks that would affect the volume of segmented puncta if a fixed threshold was applied across images, and avoided the potential subjective bias of setting a user-defined arbitrary threshold value separately for each image. Intensity per synaptic punctum was calculated as the summation of pixel intensities within the surface object. To associate the intensities of puncta belonging to the same synapse, we generated surface objects from a 4$^{th}$ channel calculated in Imaris as the sum of the three channels (GluA2, 3, and 4; or CtBP2, GluA2, and GluA4). Each of these 4$^{th}$-channel objects contained the entire synapse (presynaptic and postsynaptic elements). The summated pixel intensities for each of the three fluorescence channels were calculated within each synapse. Some synapses appeared to lack a presynaptic ribbon. The CtBP2 channel was used to make surface objects of ribbons. These ribbon objects were used to remove ribbonless synapses from the 4th-channel objects by eliminating 4$^{th}$-channel objects with centers further than 0.1 μm from the center of the nearest ribbon. The average density of synaptic fluorescence per image was calculated as median punctum intensity (a.u.) divided by median punctum volume (μm$^3$) using surface objects calculated from corresponding individual fluorescence channels.

## Airyscan confocal microscopy and image analysis

Airyscan volumes were acquired with 16-bit images, 46 μm wide containing approximately 5 IHCs, on a Zeiss LSM 880 Confocal with Airyscan, with a 100X 1.5 NA oil objective lens with a Z-step of 0.168 μm and pixel size of 26 nm in X and Y, and a pinhole setting of 1.5 AU. We collected stacks near tonotopic characteristic frequencies of 11, 20, 25, 38, 57, and 70 kHz using identical acquisition settings for all images. For display only, the brightness and contrast levels were adjusted linearly for visual clarity. Image analysis was performed on unadjusted data after Airyscan Processing.

To quantify changes in the relative abundance of GluA2 and GluA4 around individual synapses, 3-dimensional data were reduced to 1-dimensional normalized radial distributions of fluorescence density ratios around the synapse center. Analysis was performed blinded on the maximum intensity Z-projections for spatially isolated synapses only (i.e., synapses having no overlap with other

synapses XY or Z). The 2-dimensional centroid of the synaptic ribbon was defined as the synapse center. Radial distributions of normalized GluA4: GluA2 fluorescence density ratio as a function of distance from the synapse center were constructed with custom code in MATLAB Software. For each fluorescence channel, the sum of pixel intensities was calculated for a 3 x 3 pixel box (78 × 78 nm) centered on the ribbon centroid and then for 11 shells around the center box, with each shell expanding by 2 pixels (52 nm) on each side, such that the first shell was outlined by a square with dimensions of 7x7 pixels (182 × 182 nm) and the largest shell was outlined by a square of 47x47 pixels (1,222 x 1,222 nm). For each shell, the area was calculated as the number of pixels, and the sum of pixel intensities was divided by the area to calculate the 'shell density' (intensity/area) for each fluorescence channel. For each isolated synapse in an image, the GluA4: GluA2 radial distribution of the 'ratio of raw shell densities' was calculated as the blue shell density divided by the green shell density. The peak-normalized shell densities for each synapse were calculated by normalizing to the maximum shell density of each fluorescence channel such that each radial distribution of 'normalized shell density' peaked at value = 1. Then, the GluA4: GluA2 'ratio of peak-normalized shell density' was calculated for each shell of each synapse by dividing the peak-normalized blue fluorescence shell density by the peak-normalized green fluorescence shell density. The average radial distribution for each image was calculated as the mean of the individuals. Group averages for $GluA3^{WT}$ and $GluA3^{KO}$ across CF regions were calculated as the mean of image-means. Shells were transformed to 26 nm bins and values were plotted as a function of increasing distance from the synapse center.

For the GluA4:GluA2 fluorescence ratios in nanodomains within synapses, each synapse was divided into 9 matrices of 13x13 pixels, with eight matrices around one center matrix centered on the ribbon centroid. Thus, each nanodomain matrix was $338^2$ nm,$^2$ and each 9-matrix synapse (3x3 matrices) covered an area of $1{,}014^2$ nm.$^2$

### Transmission electron microscopy (TEM)

A total of 8 mice (2 per genotype either in quiet or ambient) at P35 were anesthetized with a mixture of ketamine (60 mg/kg) and xylazine (6.5 mg/kg) and were transcardially perfused with 0.1 M phosphate buffer (PB) pH = 7.2, followed by the fixative containing a mixture of 3% PFA and 1.5% glutaraldehyde in 0.1 M PB. Cochleae were dissected, fixed overnight at 4°C, decalcified in 10% ethylenediaminetetraacetic acid (EDTA) for 24–48 h at 4°C, and processed for osmication, dehydration, and embedding in epoxy resin using a similar method as previously described.[6] A series of 15–20 ultrathin serial sections (70–80 nm in thickness) of the mid-cochlea (20kH) were cut with a Leica EM UC7 ultramicrotome and collected on single slot gold-gilded grids with formvar. The ultrathin sections were viewed under a transmission electron microscope (TEM; JEOL Ltd., Akishima Tokyo, Japan) and IHC-ribbon synapses of modiolar and pillar side were imaged (at x40,000 magnification) with an Orius SC200 CCD camera (Gatan Inc, Warrendale, PA, USA). Only, IHC-ribbon synapses that were clearly located either on the modiolar or the pillar side of the IHC were used for further ultrastructural analysis.

### Morphometric analysis of TEM micrographs

A total of 70 ($GluA3^{WT}$ $n = 35$, $GluA3^{KO}$ $n = 35$) IHC-ribbon synapses were used for the 3D analysis of the surface area and volume of the postsynaptic density (PSD) and the presynaptic ribbons. The TEM micrographs were calibrated, aligned, and reconstructed using the Reconstruct software (https://synapseweb.clm.utexas.edu/software-0) as we previously described.[6,62] Additionally, in 27 ($GluA3^{KO}$) and 31 ($GluA3^{WT}$) IHC-ribbon synapses we analyzed the ribbon major and minor axes, the ribbon circularity and roundness, the PSD length, and synaptic vesicles (SVs) size from a representative TEM image of IHC-ribbon synapses using NIH ImageJ software (https://fiji.sc/) as described.[6] SVs size was calculated as (Major diameter + Minor diameter)/2. Four to six SVs were analyzed per synapse, and the grand mean was used to compare the size of modiolar and pillar side SVs. We used the ratio of the ribbon's major and minor axes to analyze the ribbon shape. The major/minor axes ratio denotes the shapes of the ribbons regardless of the size. Each ribbon's ratio was classified into six groups, from 1 to 1.5 to >3.5. When a ribbon's major/minor axes ratio is one, it represents a round shape, while the higher major/minor ratio represents a comparatively more elliptical shape. The presence of mitochondria in the afferent terminals of $GluA3^{WT}$ and $GluA3^{KO}$ in quiet was analyzed in 40 (modiolar: $n = 25$; pillar $n = 15$) and 43 (modiolar: $n = 29$; pillar $n = 14$) representative micrographs, respectively.

Representative electron micrographs of $GluA3^{WT}$ ($n = 20$) and $GluA3^{KO}$ ($n = 38$) in ambient were used to determine the average gray value (AGV settings: black = 0 and white = 255) per $\mu m^2$ of afferent terminal cytoplasm, and afferent circularity and roundness with NIH ImageJ.

## QUANTIFICATION AND STATISTICAL ANALYSIS

All the statistical analyses were conducted with GraphPad Prism software (version 9.4.1) or IGOR Pro (version 7.08, WaveMetrics). ABR comparisons were made with two-way mixed ANOVAs followed by Šidák's multiple comparisons. Two-tailed Mann–Whitney U-test with Holm- Šidák's correction for multiple comparisons or two-tailed unpaired t-tests were used to compare two independent groups. Two one-dimensional probability distributions were compared with the Kolmogorov–Smirnov (KS) test. For pairwise comparisons between more than two groups, one-way ANOVAs were used, followed by Tukey's post-hoc correction test. The Spearman rank-order correlation coefficient was used to test the strength of the association between the two variables. Statistical significance for all the tests was set to $p < 0.05$. Data are represented as mean ± standard deviation (±SD).